X-ray properties of X-CLASS-redMaPPer galaxy cluster sample: The luminosity-temperature relation

Mona Molham, Nicolas Clerc, Ali Takey, Tatyana Sadibekova, A.B. Morcos, Shahinaz Yousef, Z.M. Hayman, Maggie Lieu, Somak Raychaudhury, Evelina R. Gaynullina

Monthly Notices
of the
ROYAL ASTRONOMICAL SOCIETY
MNRAS **494,** 161–177 (2020) doi:10.1093/mnras/staa677

X-ray properties of the X-CLASS-redMaPPer galaxy cluster sample: the luminosity–temperature relation

Mona Molham [1,2★] Nicolas Clerc,[3] Ali Takey,[1,4] Tatyana Sadibekova,[5,6] A. B. Morcos,[1] Shahinaz Yousef,[2] Z. M. Hayman,[2] Maggie Lieu [7] Somak Raychaudhury [8] and Evelina R. Gaynullina[6]

[1]*National Research Institute of Astronomy and Geophysics (NRIAG), 11421 Helwan, Egypt*
[2]*Astronomy and Meteorology Department, Faculty of Science, Cairo University, 12613 Giza, Egypt*
[3]*IRAP, Université de Toulouse, CNRS, CNES, UPS (Toulouse), France*
[4]*Hiroshima Astrophysical Science Center, Hiroshima University, 1-3-1 Kagamiyama, Higashi-Hiroshima, Hiroshima 739-8526, Japan*
[5]*Laboratoire AIM, CEA/DSM/IRFU/SAp, CEA Saclay, 91191 Gif-sur-Yvette, France*
[6]*Ulugh Beg Astronomical Institute of Uzbekistan Academy of Science, 33 Astronomicheskaya str., Tashkent, UZ-100052, Uzbekistan*
[7]*European Space Astronomy Centre, ESA, Villanueva de la Caada, E28691 Madrid, Spain*
[8]*Inter-University Centre for Astronomy and Astrophysics, Pune 411007, India*

Accepted 2020 March 5. Received 2020 March 4; in original form 2019 December 2

ABSTRACT

This article presents the results of a spectroscopic analysis of the X-CLASS-redMaPPer (XC1-RM) galaxy cluster sample. X-CLASS is a serendipitous search for clusters in X-ray wavebands based on the *XMM–Newton* archive, whereas redMaPPer is an optical cluster catalogue derived from the Sloan Digital Sky Survey (SDSS). The present sample comprises 92 X-ray extended sources identified in optical images within 1 arcmin separation. The area covered by the cluster sample is ~ 27 deg^2. The clusters span a wide redshift range ($0.05 < z < 0.6$) and 88 clusters benefit from spectrosopically confirmed redshifts using data from SDSS Data Release 14. We present an automated pipeline to derive the X-ray properties of the clusters in three distinct apertures: R_{500} (at fixed mass overdensity), $R_{\rm fit}$ (at fixed signal-to-noise ratio) and $R_{300\,\rm kpc}$ (fixed physical radius). The sample extends over wide temperature and luminosity ranges: from 1–10 keV and from 6×10^{42} to 11×10^{44} erg s^{-1}, respectively. We investigate the luminosity–temperature (L–T) relation of the XC1-RM sample and find a slope equal to 3.03 ± 0.26. It is steeper than predicted by self-similar assumptions, in agreement with independent studies. A simplified approach is developed to estimate the amount and impact of selection biases that might be affecting our recovered L–T parameters. The result of this simulation process suggests that the measured L–T relation is biased to a steeper slope and higher normalization.

Key words: galaxies: clusters: general – galaxies: clusters: intracluster medium – X-rays: galaxies: clusters.

1 INTRODUCTION

Studies of galaxy clusters at high energies have developed rapidly over the last decade by harvesting X-ray mission archives and thanks to dedicated X-ray missions targeting extragalactic sources over large portions of the sky. Clusters are the most massive luminous ($\sim 10^{43}$–10^{45} erg s^{-1}) gravitationally bound structures in the Universe. They are dominated by hot gas (intracluster medium), galaxies, active galactic nuclei (AGN) and dark matter. The hot intracluster medium (ICM) emits X-ray photons via free–free and line emission, which makes them unambiguously detected as extended X-ray sources up to high redshifts. Galaxy clusters are established sensitive probes of the underlying cosmological model of our Universe (Reiprich & Böhringer 2002; Voit, Kay & Bryan 2005; Vikhlinin et al. 2009b; Rozo et al. 2010; Allen, Evrard & Mantz 2011; Sehgal et al. 2011). One of the first X-ray catalogues of galaxy clusters was the *Einstein Observatory* Extended Medium Sensitivity Survey (EMSS) catalogue (Gioia et al. 1990), assembled by serendipitous searches of data acquired by the *Einstein Observatory*. Subsequently, many cluster samples were detected from the *ROSAT* mission, both in pointed observations and in its all-sky survey (Vikhlinin et al. 1998; Böhringer et al. 2000; Böhringer et al. 2004; Horner et al. 2008).

With the advent of new-generation X-ray satellite missions like *XMM–Newton* and *Chandra*, an increased number of clusters

★ E-mail: monamolham@nriag.sci.eg

were discovered in novel areas of the mass–redshift plane. New projects were triggered, among them numerous surveys exploiting their archive databases: for instance XMM CLuster Archive Super Survey (X-CLASS; Clerc et al. 2012), 2XMMi/SDSS (Takey, Schwope & Lamer 2014; Takey et al. 2016), the XMM Cluster Survey (XCS; Lloyd-Davies et al. 2011; Mehrtens et al. 2012) and dedicated connected wide-area surveys such as Cosmic Evolution Survey (COSMOS; Finoguenov et al. 2007), XMM-Newton-Blanco Cosmology Survey (XMM-BCS; Šuhada et al. 2012), the XMM Large Scale Structure survey (XMM-LSS) (Pierre et al. 2004; Pacaud et al. 2006, 2007) and the XXL survey (Pierre et al. 2016; Pacaud et al. 2016).

Under the assumption that galaxy clusters are self-similar objects, the formation process of which is dominated by gravity, Kaiser (1986) found that the correlations among X-ray cluster observable properties are described by a power law. The X-ray luminosity–temperature (*L*–*T*) relation is one of the most investigated of such scaling relations (Pratt et al. 2009; Mittal et al. 2011; Maughan et al. 2012; Takey et al. 2019) and it is found that the slope of the relation is steeper than the self-similar prediction (which is equal to two). This is explained by non-gravitational physical processes, such as AGN heating and supernova feedback. Determining the contribution of each process to the observed deviation from self-similarity calls for refined modelling and most often for numerical simulations. Furthermore, the inevitable Malmquist and Eddington biases affect the measurement of scaling relations, so that selection effects should be taken into consideration to understand their form and evolution fully (Pacaud et al. 2007; Mantz et al. 2010a, 2010b). Malmquist bias in particular arises due to the fact that, at greater distances, one can detect high-luminosity sources in larger proportions than low-luminosity ones. Therefore, if a sample is limited in flux, higher luminosity sources appear overrepresented. Several authors designed approaches correcting for the effects arising from different selection biases specific to a survey (e.g. Pratt et al. 2009; Vikhlinin et al. 2009a; Mantz et al. 2010b; Clerc et al. 2014; Lovisari, Reiprich & Schellenberger 2015; Bharadwaj et al. 2015; Giles et al. 2016; Zou et al. 2016).

In this article, we present for the first time X-ray spectral properties of the XC1-RM galaxy cluster sample (Sadibekova et al. 2014) measured within three different apertures and the automated procedure that we embrace in this study. We investigate the observed *L*–*T* relation of the cluster sample and describe the simulation procedure adopted to probe the Malmquist bias effect on the observed *L*–*T* relation, then we interpret the results.

This article is organized as follows. In Section 2, we discuss the cluster sample, data reduction, data analysis and derivation of the temperature of intracluster gas in different apertures. In Section 3, we present the results of the *L*–*T* relation in the (0.5–2.0) keV energy band, bolometric luminosities and the simulation approach for assessing the Malmquist bias affecting our observed *L*–*T* relation. A discussion and summary of the key results are provided in Sections 4 and 5, respectively. Throughout this article, we assume a flat cosmological model with matter density $\Omega_{\rm m} = 0.3$, dark energy density $\Omega_{\wedge} = 0.7$ and Hubble constant $H_0 = 70$ km s^{-1} Mpc^{-1}, unless stated otherwise.

2 GALAXY CLUSTER SAMPLE AND DATA PROCESSING

In Section 2.1, we describe the construction of the data sample. The procedure to determine spectroscopic redshifts is described in Section 2.2 and we summarize the data reduction procedure in Section 2.3. The method to define cluster emission radii and the spectral analysis process are presented in Sections 2.4 and 2.5, respectively.

2.1 Galaxy cluster sample

The X-CLASS-redMaPPer (XC1-RM) cluster sample (Sadibekova et al. 2014) is a joint sample between X-CLASS and redMaPPer catalogues in the X-ray and optical bands, respectively, using the best overlap between two survey footprints, which covers an area of 27 deg^2. The X-CLASS catalogue[1] (Clerc et al. 2012) embraces 845 class 1 (C1) X-ray-selected galaxy clusters (C1 definition, Section 2.3) detected in 2774 *XMM* archival observations by 2010 May. The redMaPPer catalogue in the optical waveband is based on the red-sequence cluster finder algorithm, which was applied to SDSS DR8 (Rykoff et al. 2014). For this study, we use the best joint X-optical sample of 92 clusters with positional matching within an aperture of 1 arcmin. Accurate individual X-ray measurements have been provided for each cluster to ensure the best source position and an optimal masking of other field detections. Then, for the best flux estimate, a circular aperture around the X-ray source position was tuned in a semi-automatic manner from the net count rate (Clerc et al. 2012), where the count rate (count s^{-1}) is the mean number of photons collected by the telescope from the X-ray source in the direction of the optical axis in 1 second.

The cluster redshift z_λ is photometric and provided from the redMaPPer catalogue. The range of redshifts and total count rate spanned by our cluster sample are $0.05 < z < 0.6$ and 0.03–1.4, respectively. Fig. 1 shows the total counts and the photometric redshift (z_λ) distribution of the clusters in our sample.

2.2 Galaxy cluster sample with spectroscopic redshift in SDSS-DR14

The Sloan Digital Sky Survey fourteenth data release (SDSS-DR14) was released on 2017 July 31. The important class of data for our study is the spectroscopic data, more than four million spectra, which are optical spectra from (SDSS/SEGUE/BOSS/SEQUELS/eBOSS). It is the first release of data from the SDSS component extended Baryon Oscillation Spectroscopic Survey (eBOSS), including spectra from the eBOSS subprograms (SPIDERS) survey (Abolfathi et al. 2018). We ran a query to search SDSS-DR14 for spectroscopic redshifts ($z_{\rm s}$) for our list of clusters. We searched for galaxies that have $z_{\rm s}$ around each cluster X-ray position in a circle of radius 17 arcmin, which equals a physical radius of 1 Mpc at redshift 0.05. That step was made through a SQL-based interface to the Catalog Archive Server (CAS) database, where we fetched a table containing RA, Dec., source name, $z_{\rm s}$ and its uncertainty for all galaxies. The first criterion aims to present all possible results to a lower redshift limit of 0.05 for a physical radius of 1 Mpc; we will then identify the real members in each cluster. We found only 90 cluster that have galaxies with $z_{\rm s}$. Secondly, around each cluster X-ray position we accepted only galaxies with $z_{\rm s}$ within a physical radius of 1 Mpc based on the photometric redshift (z_λ), which justifies the condition of having $z_\lambda - 0.04(1 + z_\lambda) < z_{\rm s} < z_\lambda + 0.04(1 + z_\lambda)$. This redshift range was suggested in Wen, Han & Liu (2009) and Takey, Schwope & Lamer (2013) and we used it to include most galaxies with $z_{\rm s} \approx z_\lambda$. After the previous step, the list shortened to just 88 clusters that have galaxies with $z_{\rm s}$ and for each

[1] http://xmm-lss.in2p3.fr:8080/l4sdb/

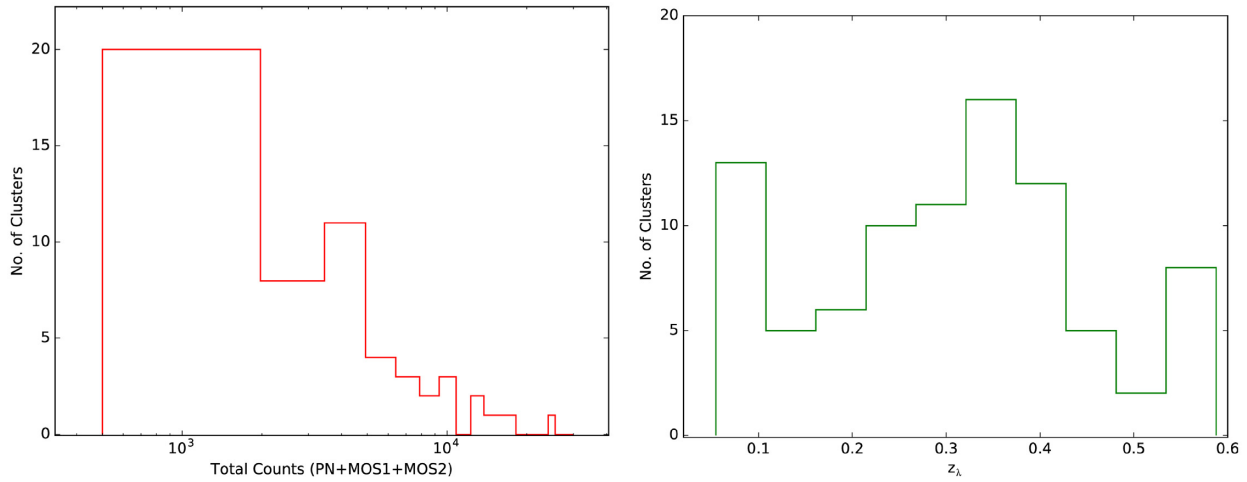

Figure 1. The distribution of net counts and redshifts of the XC1-RM galaxy cluster sample. Left: the total count (PN+MOS1 + MOS2) distribution of galaxy clusters in the XC1-RM sample. Right: the photometric redshift (z_λ) distribution of galaxy clusters in the XC1-RM sample. A colour version is available online.

cluster we calculated the weighted average of the z_s of its galaxies, where the weighted average $= \sum w z_s / \sum w$, $w = 1/(\Delta z_s)^2$. About 40 per cent of clusters have more than 10 galaxies with z_s. The relative change between z_λ and z_s is, on average, equal to 0.0025, which shows that z_λ is in good agreement with z_s (Table A1). Finally, we have 88 clusters with spectroscopic redshifts and for the remaining four clusters we used the photometric redshift z_λ obtained from Sadibekova et al. (2014), since we did not find any spectroscopic redshifts z_s in the Nasa/IPAC Extragalactic Database (NED).

2.3 Filtering and processing of *XMM* observations

The filtered event lists and other complementary files were created based on the XMM-LSS pipeline developed by Pacaud et al. (2006). The main steps are summarized in Clerc et al. (2012) and we will recall them in the next points. (i) The calibrated event lists of the three EPIC cameras (PN, MOS1 and MOS2) were generated using the *XMM–Newton* 'Scientific Analysis System' (SAS) tasks **emproc** and **epproc**. They were then filtered from high-background periods to produce images. (ii) The images created were coadded and filtered in wavelet space, then sources were detected by running SEXTRACTOR (Bertin & Arnouts 1996) on them. (iii) The XAMIN pipeline (a maximum-likelihood profile fitting procedure) provided the detected sources with a number of parameters describing their properties. The C1 sample contains clusters characterized with parameters EXT > 5 arcsec, EXT_STAT > 33 and EXT_DET_STAT > 32, namely the extension, extension likelihood and detection likelihood, respectively (Pacaud et al. 2006; Faccioli et al. 2018). It has been confirmed from simulations that the C1 class is highly free from contamination by spurious detections or misclassified point-like sources (Pacaud et al. 2007; Clerc et al. 2012).

We updated the current calibration files (CCF) and used an updated (SAS) package (version 15.0.0) rather than the package used in the preceding steps. This was proceeded by an automated pipeline using PYTHON to update and create the files required for the analysis.

2.4 Defining galaxy cluster radii and masking other field sources

The circular aperture for each cluster was defined by a semi-interactive procedure developed in section 2.4 of Clerc et al. (2012). Through that procedure, we determined the radii corresponding to the cluster emission extent, namely $R_{\rm fit}$. Firstly, count-rate measurements were performed in three energy bands: [0.5–2], [0.5–1] and [1–2] keV. The count rate is defined as the mean number of cluster photons collected by the three detectors in one second. Some manual redefinition was allowed in the case of adjustment of the cluster position centre obtained by XAMIN and accounting for the presence of a CCD gap or detector borders in the cluster emission. Secondly, the cluster was assumed to be spherically symmetric and corrected from vignetting and CCD defects. The count rates were measured in concentric annuli using the full pointing exposure to ensure a maximum signal-to-noise ratio (S/N). Another annulus was chosen at a reasonable distance far from the cluster to account for local variation. It was modelled by a photon background and flat particle background components. The uncertainties in the two parameters of the background and the cluster count rates are derived assuming Poisson noise. Thirdly, we calculated a total count rate by combining each detector count-rate measurement and using the total cluster exposure to improve the S/N. Finally, a count-rate growth curve as a function of cluster radius was computed from the total count rate (see Fig. 2) and $R_{\rm fit}$ (the cluster radius) was chosen at the point where the cluster emission merges in the background (the background is where S/N equals 1).

The segmentation map is an image with patches representing the pixels ascribed to each source in the observation. It is created by running the SEXTRACTOR software (Bertin & Arnouts 1996) on the wavelet-filtered images (Clerc et al. 2012). It was used in the XAMIN procedure to omit pixels belonging to other sources that obscure the source of interest.

We created a mask out of the segmentation map for each cluster to mask all sources in the field of view except the cluster of interest. The segmentation maps for a few cases were edited manually. The patches on the segmentation map might need to be merged together upon visual inspection. There are 11 clusters with modified segmentation maps; we ran all the steps aforementioned to modify the mask created for them accordingly.

The process was performed fully using an automated PYTHON pipeline and then checked manually. Images of the masks with the cluster aperture and background annulus overlying correspondingly for each observation (see Fig. 3) were created and evaluated by visual inspection. We omitted clusters with background annuli

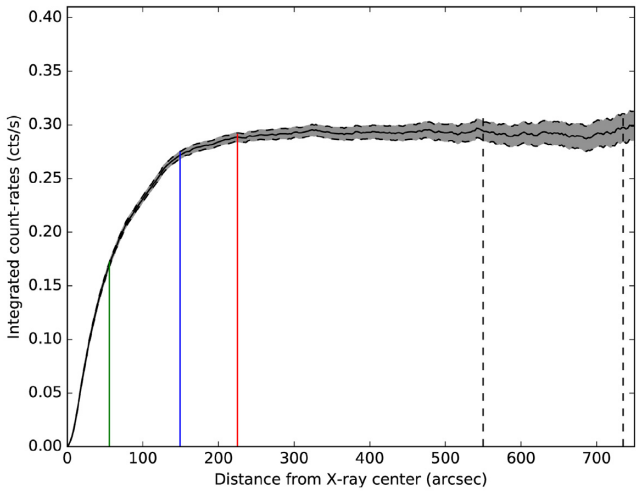

Figure 2. The net count rate (PN+MOS1+MOS2) growth curve of the cluster X-CLASS 377; the grey area represents the 1σ error bar. $R_{300\,\mathrm{kpc}}$, R_{500} and R_{fit} are represented by the green, blue and red lines, respectively. The dashed vertical lines indicate the region we used for the background annulus. A colour version is available online.

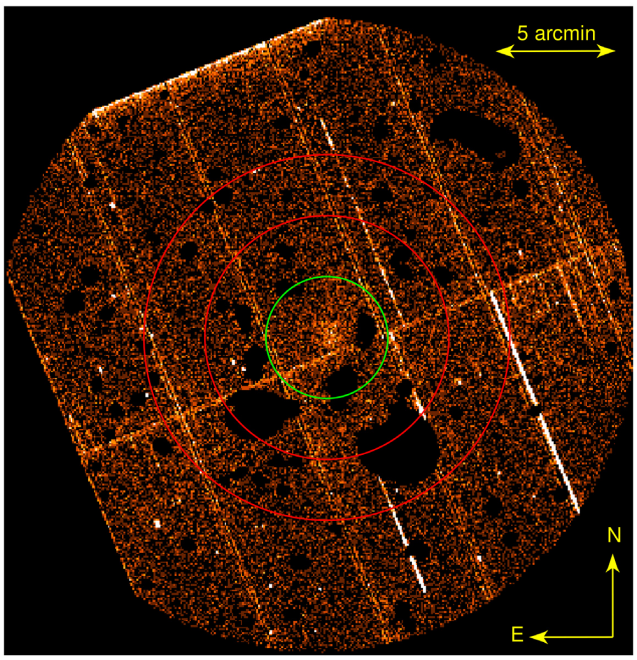

Figure 3. The PN image of the cluster X-CLASS 1059. It is overlaid by the cluster extent circle (R_{fit} = 112.5 arcsec) in green and the background annulus in red. The image is multiplied by the segmentation mask, where black colours represent excluded areas. A colour version is available online

larger than the field of view (e.g. bright and nearby clusters); more details can be found in Section 2.5.2.

2.5 Spectral analysis

Cluster spectra are extracted from the three EPIC cameras, except for one cluster (X-CLASS 2295), which was on the damaged CCD6 of MOS1. The procedure was performed by **especget** (SAS task to generate all necessary files for the spectral fitting of *XMM* sources) and the fitting is performed in the 0.3–7.0 keV band. We developed a procedure that uses the mask created out of the segmentation map, the cluster radius and the background annulus in **especget** to create a spectrum representing genuine cluster emission with no contamination by nearby sources. The background annulus has an inner radius that is twice the cluster radius (R_{500}, R_{fit} , $R_{300\,\mathrm{kpc}}$) and an outer radius triple that value.

For spectral fitting, we utilized the XSPEC package (12.9.1t: Arnaud 1996), where each cluster spectrum was fitted with a single-temperature APEC (ATOMDB-VERSION 3.0.7) plasma model multiplied by TBABS (Tübingen–Boulder absorption model by Wilms, Allen & McCray 2000) and assuming a fixed galactic hydrogen column density given by Kalberla et al. (2005). The photon counts of each cluster spectrum were grouped into bins with at least one count per bin, as recommended in Krumpe et al. (2008) for X-ray spectra, using the FTOOLS task **grppha**, and we used Cash statistics (Cash 1979) for fitting the model, due to the Poissonian nature of the noise.

The spectra for the three cameras were fitted simultaneously with the temperature parameters tied together, and all the errors quoted here are with their 1σ errors. The solar abundance was fixed at 0.3 $Z_{\odot}$ and redshifts were described in Section 2.2. We calculated the flux and luminosity in the energy band [0.5–2.0] keV. It is not straightforward to calculate the unabsorbed luminosity within its uncertainties while keeping all other parameters at their fitted value, so we used the new convolution model **clumin**. It gives the unabsorbed luminosity and uncertainties for the selected model without changing other parameters (i.e. the column density parameter is not equal to zero). We determined the bolometric luminosity of the cluster rest frame, in the energy band [0.01–100.0] keV, from a dummy response matrix created by the best-fitting model and its parameters. All errors represent 68 per cent of the confidence range.

All the spectra extracted within different apertures follow the same fitting process; below, we will describe the three apertures used in our analysis.

2.5.1 R_{500} measurements

R_{500} is defined as the cluster radius embrace mass density equals 500 times the critical density of the Universe at the cluster redshift. We used the empirical equation

$$E(z)R_{500} = r3(T_{500}/3\,\mathrm{keV})^{\alpha/3}),\ E(z) = (\Omega_{\mathrm{M}} \times (1+z)^3 + \Omega_{\Lambda})^{1/2} \quad (1)$$

for the (Tier 1+2 + clusters) sample in Sun et al. (2009) to obtain the R_{500} value. The values $r3 = 0.600$ and $\alpha = 1.65$ are from table 6 of Sun et al. (2009) and z is the redshift value of our cluster sample.

We started the iteration procedure with an initial temperature value equal to 2.0 keV. First, we calculated R_{500} from equation (1). Secondly, we used the R_{500} obtained from the previous calculation to create new spectra and background files. We did not generate a new response matrix and ancillary response files yet; we used existing files from the same cluster. Thirdly, we computed the temperature through XSPEC. We used the same spectral analysis approach we followed in Section 2.5. Finally, we used the new temperature we obtained from XSPEC to calculate a new R_{500} value using equation (1).

We set the next condition to check the output results and to determine how long the iteration process will last for one cluster, also the results for each iteration step are preserved. We start with five iterations and create a representative plot (see Fig. B1), then we check if any of these iterations changes by less than 0.01 of its precedent. Whether this condition is reliable or not, we run five more iterations and create a representative plot of all ten iterations, then we check the previous condition again. If that condition is valid, we choose the lowest value (below 0.01) that represents a steady behaviour among R_{500} values in the iteration steps and also shows consistency with their uncertainty range in the plot; the iteration process then halts and moves to the next cluster. If the previous condition is not true, we run five more iterations and create a representative plot and again check if the condition valid, then the iteration process halts and moves on to the next cluster. If the condition failed, then we consider this a failed case and move to the next cluster.

Out of the 92 clusters, we managed to calculate R_{500} within the range 0.5–1.24 Mpc for 57 clusters (Table A2). The total counts range between 250 and 2.14×10^5, with a median value equal to 3820. Also, we calculated the bolometric and band [0.5–2.0] keV luminosity for them. The remaining 35 clusters failed because they did not fulfil the condition required to pass through the pipeline.

2.5.2 R_{fit} measurements

The cluster temperature measured within $R_{\rm fit}$ is called $T_{\rm fit}$ and we were able to derive the temperature for 68 clusters of the cluster sample (Table A3), which have total counts ranging between 145 and 3.2×10^4 and a median value equal to 2600. Two clusters with unconstrained errors in temperature measurement (X-CLASS 1185, X-CLASS 1813) are removed from the $R_{\rm fit}$ sample. The remaining 22 clusters are classified as bright and nearby clusters with a high chance of being studied in the literature, since their circular aperture covers the image fully and their background annulus extends outside it. It might be surprising that we could not manage to calculate the temperature within $R_{\rm fit}$ for the clusters (X-CLASS 458, X-CLASS 2202, X-CLASS 2211) while they are already have temperature measurements within R_{500}, but it happened that they reached a stable R_{500} lower than $R_{\rm fit}$, so it was possible to obtain their temperature measurements.

We found 14 of these bright and nearby clusters with studies using the *XMM* mission, six of them with studies using other X-ray missions and two with no studies at all (Table A5). For some cases of these 22 clusters, we measured temperatures very close to the values found in the literature.

2.5.3 $R_{300\,\rm kpc}$ measurements

We also derived the temperature within a fixed aperture of 300 kpc and were able to derive the temperature within this aperture for 87 clusters (Table A4) with total counts in the range 125–2.7×10^5 counts and a median value equal to 2410 counts. Five clusters (X-CLASS 1307, X-CLASS 1185, X-CLASS 535, X-CLASS 2130, X-CLASS 2209) are removed from the $R_{300\,\rm kpc}$ sample because they have unconstrained errors in their temperature measurements. It is worth noting that we managed to derive the temperature for the cluster (X-CLASS 1307) using $R_{\rm fit}$. Also, we found that using the chi-squared (chi) fit statistic instead of Cash statistics gave an acceptable temperature for that cluster (X-CLASS 1307) within an aperture of 300 kpc.

Table 1. Categorization of the clusters in each aperture (R_{500}, $R_{\rm fit}$, $R_{300\,\rm kpc}$).

Aperture	Number of sources	Succeed cases	Fail cases	Literature
R_{500}	92	57	35	02‡
$R_{\rm fit}$	92	68	02	22
$R_{300\,\rm kpc}$	92	87	05	–

Note: ‡ They are also presented in the succeed cases with R_{500}.

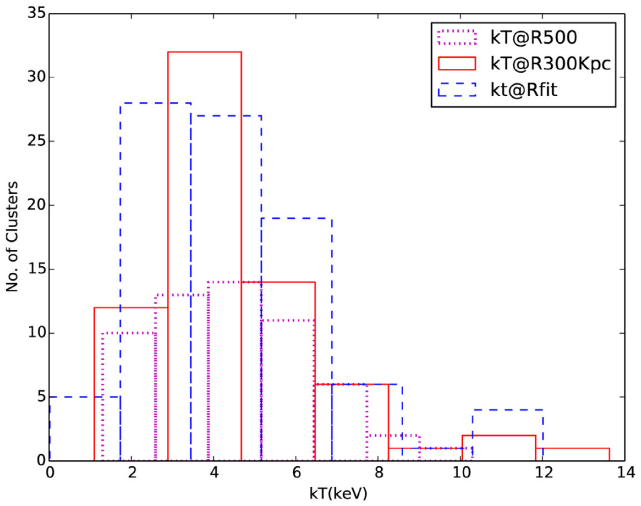

Figure 4. Temperature distribution of the galaxy clusters in XC1-RM. The temperature derived within $R_{\rm fit}$ is represented by a blue dashed line (68 clusters), that within $R_{300\,\rm kpc}$ is represented by a red solid line (87 clusters) and that within R_{500} is represented by a pink dotted line (57 clusters). The three groups peak at almost the same range of temperatures. A colour version is available online.

3 RESULTS

3.1 Temperature measurements

We discussed in Section 2.5 the procedure we followed to calculate the temperature within different apertures and a summary of the results is given in Table 1.

Our cluster sample spans a temperature range of (1.0–10 keV) within R_{500} with a peak at nearly 4.0 keV and a mean value $\sim$ 4.5 keV in the three apertures (R_{500}, $R_{\rm fit}$, $R_{300\,\rm kpc}$). The temperature distributions within R_{500}, $R_{\rm fit}$ and $R_{300\,\rm kpc}$ are shown in Fig. 4. The mean luminosities in the band [0.5–2.0] keV for our sample are 12×10^{43}, 8×10^{43} and 6×10^{43} erg s^{-1} within R_{500}, $R_{\rm fit}$ and $R_{300\,\rm kpc}$, respectively, while the mean bolometric luminosities for our sample are 4×10^{44}, 2×10^{44} and 2×10^{44} erg s^{-1} within R_{500}, $R_{\rm fit}$ and $R_{300\,\rm kpc}$, respectively.

Tables A2, A3 and A4 represent the cluster X-ray properties measured within R_{500} (57 clusters), $R_{\rm fit}$ (70 clusters) and $R_{300\,\rm kpc}$ (92 clusters), respectively. In Table A2 we present the characteristic properties of each cluster; X-CLASS ID is presented in column 1. Temperature and its negative and positive 68 per cent uncertainties are presented in columns 2, 3 and 4, respectively. The R_{500} aperture is in column 5 and the fluxes measured in band [0.5–2 keV] are in column 8. The band luminosity [0.5–2 keV] is presented in column 11. In Table A3, the first column is the X-CLASS ID, where $R_{\rm fit}$ is in column 2. Temperature and its negative and positive 68 per cent uncertainties are presented in columns 3, 4 and 5, respectively. Fluxes measured in band [0.5–2 keV] are in column 6. The band luminosity [0.5–2 keV] is listed in column 9. In Table A4, the first

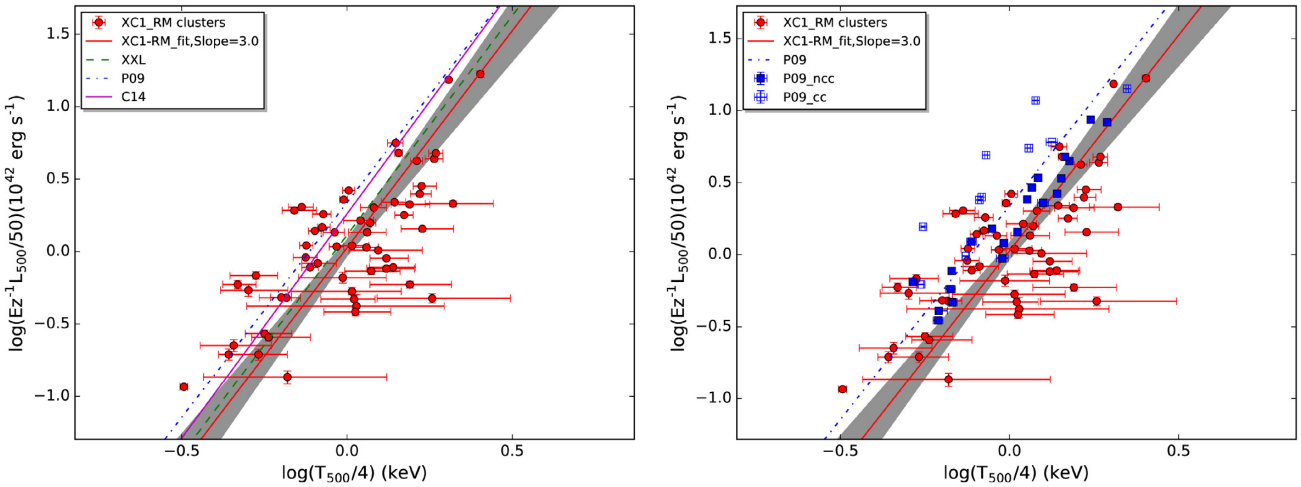

Figure 5. *L–T* relation for 57 clusters. Left: the red solid line represents the fit to our cluster sample in red points. The shaded area represents the 1σ uncertainty for our relation. The magenta solid line, green dashed line and blue dash–dotted line represent the fit to Clerc et al. (2014), Giles et al. (2016) and Pratt et al. (2009), respectively. Right: the same as the left plot, but showing the P09 sample divided into cool-core (empty blue square) and non cool-core (filled blue square). A colour version is available online

column is the same as in Tables A2 and A3, $R_{300\,\mathrm{kpc}}$ measured in arcsec is in column 2 and temperature and its negative and positive 68 per cent uncertainties are given in columns 3, 4 and 5, respectively. Fluxes and the luminosity measured in band [0.5–2 keV] are in columns 6 and 9, respectively.

For each of the 22 bright clusters in Section 2.5.2, we searched for temperature measurement results in the literature that fulfil the following conditions: the cluster core should not be excluded, it should be an *XMM* study and the temperature should be measured in a circular aperture not an annulus. Table A5 lists the results we found in the literature and their references. In Table A5, we also present our results, which we managed to calculate for some clusters. The first column represents the X-CLASS ID, while the temperatures we found in the literature with their uncertainties are presented in subcolumns 1, 2, 3 and 4, respectively. The apertures where those published temperatures are measured and the references are presented in subcolumns 5 and 6, respectively. The second column represents our results and presents our temperatures and their negative and positive 68 per cent uncertainties in subcolumns 1, 2 and 3, respectively. R_{500} is presented in subcolumn 4.

3.2 *L–T* relation

We investigated the band [0.5–2 keV] luminosity–temperature (*L–T*) relation for those clusters having R_{500} values. There are 57 clusters (Table 1, Section 2.5.1). Fig. 5 shows the *L–T* relation for our 57 clusters, along with the 1σ uncertainty. The relation was fitted by the power-law equation [$L/L_0 = E(z)^n \times b \times (T/T_0)^a$] in log space of base 10, where $n = 1$ assuming self-similar evolution, and b, a are the normalization and the slope, respectively. We used the orthogonal regression model (BCES) to fit the power-law equation to the sample and assumed that $L_0 = 5 \times 10^{43}$ erg s^{-1} and $T_0 = 4$ keV. The solid red line represents the power-law fit of our cluster sample. We found slope $a = 3.00 \pm 0.31$ and normalization $b = 1.07 \pm 0.12$. Subsequently, we compared our results with the REXCESS (Pratt et al. 2009, hereafter P09), XMM-LSS (Clerc et al. 2014, hereafter C14) and XXL (Giles et al. 2016, hereafter XXL) samples of clusters. We used our analytic expression for the *L–T* relation to fit their data using the same pivot L_0 and T_0 of our relation. The green dashed line represents the fit to the XXL sample, which gives slope $a = 3.03 \pm 0.26$ and normalization $b = 1.29 \pm 0.09$, where the blue dash–dotted line represents the fit to the P09 sample, which gives slope $a = 2.97 \pm 0.31$ and normalization $b = 2.19 \pm 0.50$. The purple solid line represents the fit to C14 sample, which gives slope $a = 3.10 \pm 0.38$ and normalization $b = 1.82 \pm 0.44$. The intrinsic logarithmic scatter of our *L–T* relation is calculated following the procedure presented by Arnaud, Pointecouteau & Pratt (2005). All the fitting parameters, along with the intrinsic scatter, are listed in Table 2.

Table 2. The *L–T* relation parameters, $L/L_0 = E(z)^n b(T/T_0)^a$, where $L_0 = 5 \times 10^{43}$ erg s^{-1} and $T_0 = 4$ keV. We used the BCES orthogonal fit method. We use the first subsample in Table 1 for all our *L–T* relations.

Cluster sample	a	b	$\sigma_{\mathrm{int,\,L}}$
XC1-RM	3.00 ± 0.31	1.07 ± 0.12	0.44 ± 0.06
XC1- RM$_{\mathrm{bol}}$	3.25 ± 0.24	2.63 ± 0.30	0.37 ± 0.05
XC1- RM$_{\mathrm{Simulated}}$	3.14 ± 0.27	1.58 ± 0.23	0.38 ± 0.05
XC1-RM$_{Z<0.3}$	2.14 ± 0.28	1.05 ± 0.19	0.18 ± 0.04
XC1-RM$_{Z>0.3}$	3.59 ± 0.54	0.91 ± 0.19	0.42 ± 0.07
XXL	3.03 ± 0.26	1.29 ± 0.09	0.40 ± 0.04
P09	2.97 ± 0.31	2.19 ± 0.50	0.34 ± 0.06
C14	3.10 ± 0.38	1.82 ± 0.44	0.37 ± 0.05

3.2.1 L_{bol} –*T* relation

Since we calculated the bolometric luminosity for the 57 clusters having R_{500} values (Section 2.5.1), we investigated their bolometric luminosity–temperature (L_{bol}–*T*) relation. The sample data were fitted using the same power-law equation used in Section 3.2. We found slope $= 3.25 \pm 0.24$, normalization $= 2.63 \pm 0.30$ and intrinsic scatter $= 0.38 \pm 0.5$, comparable with the results in Zou et al. (2016) and P09. Zou et al. (2016) studied a sample of 23 clusters and their core-included (*L–T*) relation gave slope $= 3.28 \pm 0.33$, while P09 found slope $= 3.35 \pm 0.32$ using also bolometric luminosity for the core-included sample. Fig. 6 shows the L_{bol}–*T* relation for our sample with 1σ uncertainty and the fit results are given in Table 2.

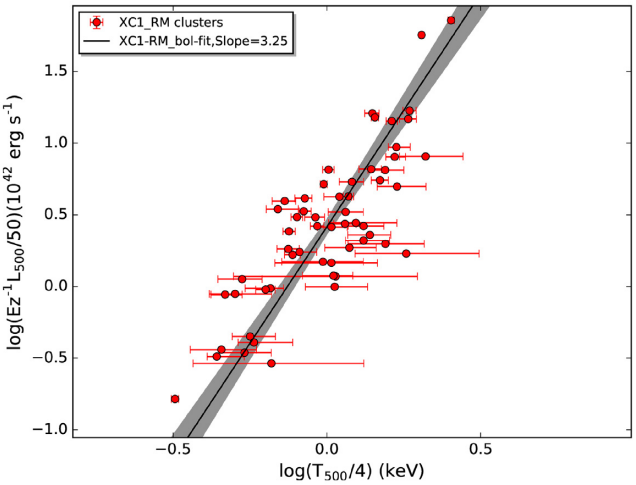

Figure 6. The $L_{\rm bol}$–T relation. The black solid line represents the fit to our sample in red points. The shaded area represents the 1σ uncertainty for our sample. A colour version is available online.

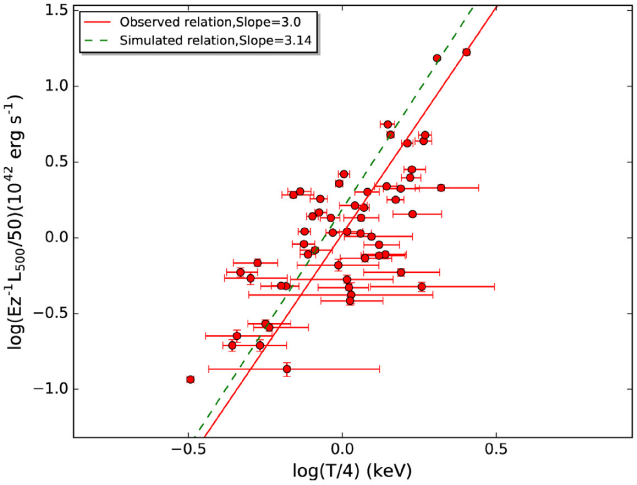

Figure 7. The observed and simulated L–T relation. The red solid line represents the fit to our sample in red points. The dashed green line is the simulated L–T relation. A colour version is available online.

3.3 Simulated *L–T* relation

We want to investigate the effect of Malmquist bias on our sample, where it would present more bright clusters in our sample than the true distribution at a given redshift (Clerc et al. 2014; Mantz et al. 2010b; Pacaud et al. 2007). Thus, we developed a simulation approach to estimate the amount of bias affecting our observed L–T relation. We created a sample of points that represents the underlying population of clusters and considered our observed band L–T relation as the unbiased relation to obtain a realization of the sample luminosities. We then applied detection constraints (e.g. flux threshold, background noise and exposure time). The simulated sample spectral properties and their uncertainties are introduced like our observed sample, and we used the BCES fit to investigate the resulting L–T relation. Below, we describe the simulation approach we followed in detail.

We created a list of 10 000 random T and z values (sample 1) distributed according to a galaxy cluster mass function (Tinker et al. 2008), WMAP5 cosmological parameters and the M–T relation from Arnaud et al. (2005). A second list of 500 000 random T and z values (sample 2) was created using the same mass function, WMAP9 cosmological parameters and a different M–T relation from Sun et al. (2009). We used our L–T relation parameters and the power-law equation in Section 3.2, $L/L_0 = E(z)^n b(T/T_0)^a$ with $b = 1.07$, a=3.0, $n = 1$, intrinsic scatter $\sigma_{\rm int,\,L} = 0.44$, $L_0 = 5 \times 10^{43}$ erg s^{-1} and $T_0 = 4$ keV, to calculate the luminosity (L) for the temperature values in the two samples.

We utilized the same XSPEC package (12.9.1t) to calculate the flux for both samples. We used a single-temperature APEC plasma model multiplied by the TBABS absorption model (Wilms et al. 2000) and assuming a fixed galactic hydrogen density column at 0.026×10^{22} cm^{-2}. The solar abundance was fixed at 0.3 $Z_\odot$ and the redshift was obtained from the two samples. The flux was calculated by changing the normalization parameter iteratively to give luminosity values nearly equal to the ones calculated from the L–T relation. The flux limits of our observed sample are above 2.48×10^{-14} erg s^{-1} cm^{-2} and below 1.5×10^{-12} erg s^{-1} cm^{-2}. We applied the same flux limit to the simulated samples, which reduced the number of the two samples to around 300 simulated points in sample 1 and 12 000 simulated points in sample 2. After that, the **fakeit** command in the XSPEC package was used to create spectra of the parameters obtained in the preceding steps. The rmf and arf in the (EPIC) thin filter used in the analysis are from the XMM online database.[2] Then, a random background file from our sample (to simulate the noise we found in the real observation) was applied and we chose an average exposure time of 15 ks (average exposure time for our sample). At that point, we created mock spectra for both samples (1 and 2). To derive temperatures and luminosities, we followed the same procedure mentioned in Section 2.5. For both samples, we generated random subsamples, where each contains 57 simulated points, to resemble the observed cluster sample. Subsequently, we plotted the luminosity versus temperature (L–T) for the subsamples and the orthogonal regression model (BCES) was applied for fitting (Section 3.2). To determine an average slope and intercept, we calculated the mean for 1000 subsamples in both samples. We found slope a =3.18 ± 0.07 and normalization b = 1.58 ± 0.22 for sample 1 and slope a =3.14 ± 0.27 and normalization b = 1.58 ± 0.23 for sample 2. The results of sample 2 are shown in Fig. 7 and Table 2.

4 DISCUSSION

In this section, we interpret our temperature measurements and luminosity–temperature relation results and compare them with other related studies in the literature. The effect of Malmquist bias on the observed L–T relation is also discussed.

4.1 Temperature measurements

In Fig. 8, we compare our results with 16 and 20 galaxy clusters from XCS-DR1 and 2XMMi/SDSS catalogues matched within 15 arcsec, respectively.

XCS-DR1 is the *XMM* Cluster Survey first data release (Hilton et al. 2012; Mehrtens et al. 2012; Lloyd-Davies et al. 2011). Hilton et al. (2012) investigated the evolution of the L–T relation for 211 clusters of XCS-DR1 with spectroscopic redshifts, where the temperature and luminosity were measured using the pipeline described in Lloyd-Davies et al. (2011). For XCS temperature measurements, our results are nearly consistent (left panel,

[2] ftp://legacy.gsfc.nasa.gov/xmm/data/responses/qd/

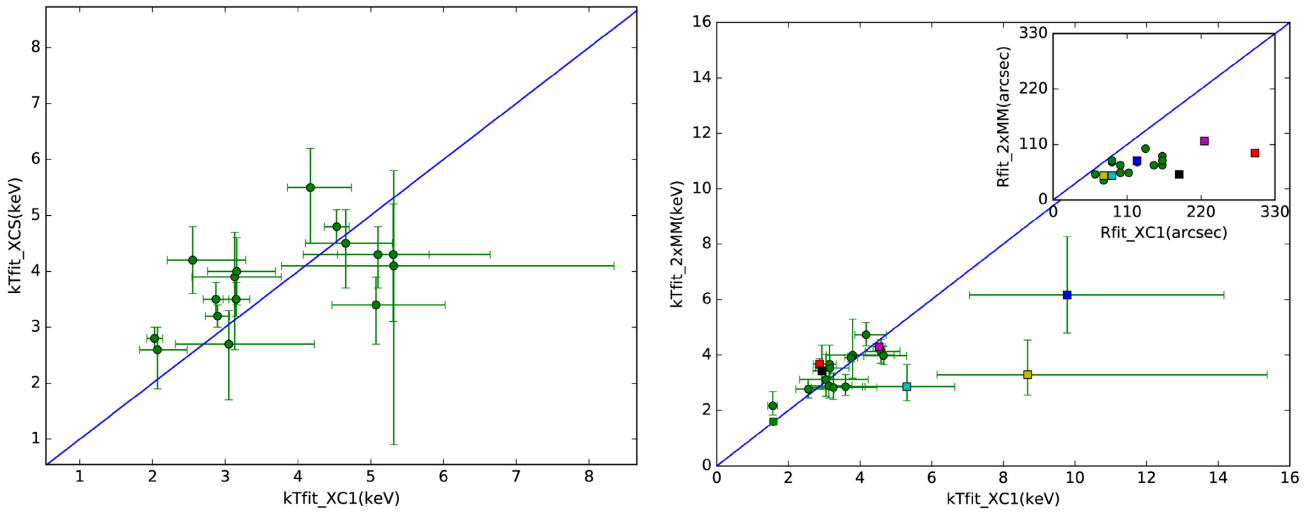

Figure 8. Temperature measurement comparison with XCS and 2XMMi/SDSS. Left: a comparison between the temperature of 16 galaxy clusters in common between XC1-RM and XCS (Hilton et al. 2012). The solid blue line shows the one-to-one relationship. Right: a comparison between the temperature of 20 galaxy clusters in common between XC1-RM and 2XMMi/SDSS (Takey et al. 2013). The solid blue line shows the one-to-one relationship and the inset is a comparison between the radii measurements of the two samples. The colour points represent the outliers on the inset plot.The errors represent 68 per cent of the confidence range. A colour version is available online.

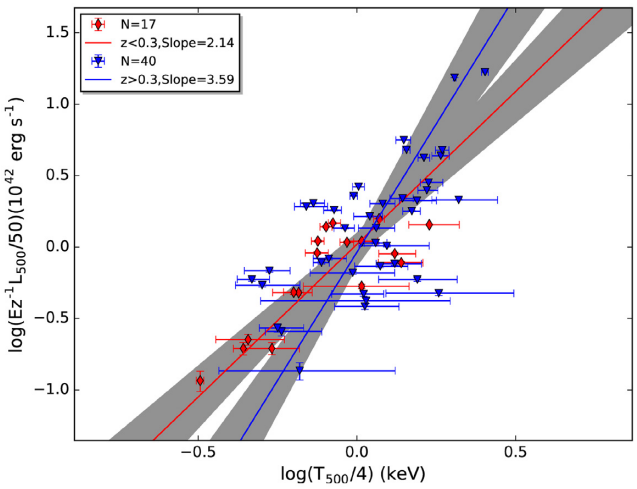

Figure 9. $L-T$ relation in different redshift bins. The red points represent clusters with redshift lower than 0.3. The blue points represent clusters with redshift higher than 0.3. The shaded area for each of the two samples represents the 1 σ uncertainty. A colour version is available online.

Fig. 8). We could not compare our $R_{\rm fit}$ with their radii measurements, but it is possible that different cluster emission apertures resulted in slightly different temperature values.

Takey et al. (2013) presented 345 galaxy clusters with temperature measured within the optimum extraction radius and bolometric luminosity measured within R_{500}. The optimum extraction radius is described as the radius representing the highest signal-to-noise ratio (S/N) point on a radial profile of the X-ray surface brightness of each cluster created in the energy band [0.5–2.0] keV on each camera (PN, MOS1, MOS2) and the combined one [Section 3.2.1 of Takey, Schwope & Lamer (2011)]. For 2XMMi/SDSS temperature measurements, our results are nearly consistent (right panel, Fig. 8) except for a few points that need more investigation. Thus, we compared the radii used in both samples, which originated from different techniques (Section 3.2.1, Takey et al. 2011; Section 4, Clerc et al. 2014). Interestingly, we found that all radii extracted in 2XMMi/SDSS are lower than the radii in our sample. Nonetheless, the temperature measurements for the clusters that have the highest difference in radius measurements are not affected (see inset, right panel, Fig. 8). This shows that using different cluster extents is not always the main reason leading to a discrepancy in temperature measurements and such a discrepancy might arise for different reasons (e.g. spectral fitting models).

Our temperature results are mostly consistent with the results in XCS-DR1 and 2XMMi/SDSS, where the existence of a few clusters having high error bars in our sample is prominent, since we do not exclude clusters with high uncertainties, similar to the XCS and 2XMMi/SDSS study. Additionally, XCS-DR1 and 2XMMi/SDSS use different spectral fitting models and different methods to determine the cluster emission extent. Our cluster sample has an average temperature of 4.0 keV in the three subclasses extracted at different radii. Similar results can be found in Giles et al. (2016) and Ebrahimpour et al. (2018).

4.2 *L–T* relation

We chose the BCES method (Akritas & Bershady 1996) because it has been widely used in other studies with which we will compare our results. The errors in temperature and luminosity were converted into a lognormal likelihood using the method of Andreon (2012). We preferred to use one BCES fitting method (BCES orthogonal), which minimizes the orthogonal distance from the data points to the fitted line.

We found a steeper slope than that was found in the self-similar expectation (∼2.0), which is in agreement with recent studies (Pratt et al. 2009; Hilton et al. 2012; Maughan et al. 2012; Lovisari et al. 2015; Giles et al. 2016; Takey et al. 2019). It has been found that cluster samples constructed without regard to their core activity, like our current sample, almost give a slope ≥3 (Mantz et al. 2010b; Clerc et al. 2014; Giles et al. 2016). Our observed L–T relation gave a =3.00 ± 0.31 and b = 1.07 ± 0.12, which is consistent

with XXL results (a =3.03 ± 0.26, b = 1.29 ± 0.09) within 1σ in normalization.

Comparing with P09, we found a normalization within 2σ of their results, which was led by the strong cool core present in their sample (right plot in Fig. 5). The P09 sample has high-luminosity clusters at redshifts $z < 0.2$ and a flux limit above 3×10^{-12} erg s^{-1} cm^{-2} (Böhringer et al. 2007), opposite to our sample, which contains low-luminosity deep clusters (flux below 1.5×10^{-12} erg s^{-1} cm^{-2}, redshifts up to 0.6). We do not know how many cool-core clusters are in our sample, since we could not excise them.

In Fig. 9 we divide our sample into two redshift bins to investigate the *L–T* parameter evolution with redshift. We found that the slope is 3.59 ± 0.54 at redshift greater than 0.3, which is almost twice the slope 2.14 ± 0.28 at redshift less than 0.3, and we found a slight change in normalization within its error range (see Table 2).

Our result does not agree with the XCS-DR1 sample (Hilton et al. 2012), where they found that the slope did not change dramatically with redshift. In XCS-DR1, they divided the sample into three redshift bins and fitted them using an orthogonal method. Compared with their first two redshift bin subsamples, which have a slope equal to 3.18 ± 0.22 in the redshift bin lower than 0.25 and a slope equal to 2.82 ± 0.25 in the redshift bin higher than 0.25, they found that the slope decreased as the redshift increased, in contrast to our findings.

On the other hand, in 2XMMi/SDSS (Takey et al. 2013), they found a slope equal to 2.55 ± 0.23 in the redshift bin below 0.25 and a slope equal to 3.27 ± 0.26 in the redshift bin above 0.25. The slope is higher in high-redshift bins, which is in accordance with our results, but they suggested that this resulted from including clusters and groups of low temperature in the low-redshift bin.

To investigate this result further, we used different redshift thresholds (e.g. z greater than 0.25 and z less than 0.25), where we found that the slope is still higher in the higher redshift bins than in the lower redshift bins.

Also, we found that the low-temperature clusters in our sample are presented in the two redshift bins, so this was not the cause of a shallower slope in the low-redshift bins. We suspect that the presence of high-luminosity and intermediate-temperature clusters is the reason for a higher slope in higher redshift bins.

4.3 Effect of Malmquist bias

We have shown that using a developed approach (Section 3.3) to investigate the Malmquist bias in the *L–T* relation produces a steeper slope than the one we found in the observed-uncorrected *L–T* relation (Fig 7). It gave a slope and normalization ($a = 3.14 \pm 0.27$, b = 1.58 ± 0.50) higher than the input parameter (a = 3.00, $b = 1.07$). Consequently, it appears that the Malmquist bias raised our *L–T* relation parameters, which means there is the possibility of finding a shallower slope, if we undertake a sophisticated approach (accounting for the biases) to correct our observed-uncorrected *L–T* relation.

Although we cannot confirm the concluded result, or make a proper comparison with other studies, we found comparable results. In XXL (Giles et al. 2016), the selection function of the survey was taken into account, where they found a shallower slope after applying the correction to the *L–T* relation. Also, in Bharadwaj et al. (2015), they found a shallower slope for HIFLUGCS galaxy clusters and their subsamples after correcting the sample biases (table 3, Bharadwaj et al. 2015). It is worth noting that, in Bharadwaj et al. (2015), the results were for a corrected bolometric *L–T* relation and they used the BCES L|T method.

It is also worth mentioning that, in Zou et al. (2016), the slope did not vary significantly after applying similar bias correction. This was attributed to the BCES regression method used, since they used BCES orthogonal over BCES L|T, where the latter minimizes the residuals in L, so it is more sensitive to selection effects.

We also investigated the probability that the inputs of the simulation approach might have a major impact on the output results. In Section 3.3 we used a different set of cosmological parameter and *M–T* relations to investigate their impact on the simulation approach. We found that changing either the *M–T* relation or the cosmological parameters had no significant impact on the simulated *L–T* relation. Furthermore, we applied a different *L–T* relation in the simulation approach; we used the XXL corrected *L–T* relation ($a = 2.63$, b= 0.71, $\sigma = 0.47$) and it gave a higher slope = 2.98 and normalization = 0.97. That investigation and the aforementioned result that we obtained in different redshift bins (Section 4.2) could present a reasonable view on the bias affecting our sample.

5 SUMMARY

In this work, we introduced the first X-ray study of the (X-CLASS-redMaPPer) sample in the X-CLASS survey, which contains 92 galaxy clusters. The sample spans a range of redshifts $0.05 < z < 0.6$. Here, we summarize our main results.

(i) Our spectral results are in a good agreement with the results in the literature. We measured the X-ray spectral properties for 92 galaxy clusters and succeeded in obtaining results for 57, 68 and 87 clusters within R_{500}, $R_{\rm fit}$ and $R_{300\,\rm kpc}$, respectively. The X-ray spectral properties were measured in a homogeneous way by an automated pipeline that we developed for this work.

(ii) For measurements within the R_{500} aperture, the sample temperature spans range from $T \simeq$ 1.0–10 keV and the band luminosity [0.5–2.0] keV ranges from $L \simeq 6 \times 10^{42}$ to 11×10^{44} erg s^{-1}. R_{500} was calculated in an automated iterative method and the procedure also created representative plots for manual checks.

(iii) We studied the X-ray luminosity–temperature (*L–T*) relation in log–log space for cluster parameters measured within R_{500}, which gave a slope = 3.00 ± 0.31, supporting studies that have a higher slope than the one expected by a self-similar model and in good agreement with similiar recent studies.

(iv) We divided the sample into two redshift bins, where we found a steeper slope in the high-redshift bin. The slope is always steeper in higher redshift bins than in lower redshift bins, opposite to what is found in the literature, indicating that the slope in higher redshift bins could be biased by the existence of high-luminosity clusters, and we will investigate this in a larger cluster sample to confirm this behaviour.

(v) We developed a simplified simulation approach to assess the amplitude of the bias affecting our *L–T* relation, where we found that the bias in our sample is moving the *L–T* relation parameters higher. There are recent studies that found such a result, but it requires further investigation.

Future investigations will determine the intracluster gas mass ($M_{\rm gas}$) of the sample. We will probe its scaling with other X-ray quantities. The impact of selection effects on the scaling relations will be assessed quantitatively by increasing the size of the sample and implementing more elaborate approaches ,taking advantage of the enhanced statistics and redshift leverage.

ACKNOWLEDGEMENTS

This work was carried out in Egypt and supported by the National Research Institute of Astronomy and Geophysics (NRIAG) through funds for short international travels. The results presented here are based on data from the X-CLASS serendipitous cluster catalogue extracted from the *XMM* archival data. Mona Molham is thankful to Faccioli Lorenzo for his help with the data sample. Mona Molham acknowledges support from IAU via air flight tickets for a short visit to The Inter-University Centre for Astronomy and Astrophysics (IUCAA). Mona Molham also thanks the (IUCAA) institute for accepting her visit and hosting for a few months. Mona Molham is thankful to Professors Ajit Kembhavi and Ranjeev Misra for their helping and guiding during the visit. My thanks to Anjlia who helped me on the **fakeit** procedure in XSPEC. This research has made use of software provided by the High Energy Astrophysics Science Archive Research Center (HEASARC), which is a service of the Astrophysics Science Division at NASA/GSFC and the High Energy Astrophysics Division of the Smithsonian Astrophysical Observatory. Funding for the Sloan Digital Sky Survey (SDSS) has been provided by the Alfred P. Sloan Foundation, the Participating Institutions, the National Aeronautics and Space Administration, the National Science Foundation, the US Department of Energy, the Japanese Monbukagakusho and the Max Planck Society. The SDSS Web site is http://www.sdss.org/. The SDSS is managed by the Astrophysical Research Consortium (ARC) for the Participating Institutions. The Participating Institutions are the University of Chicago, Fermilab, the Institute for Advanced Study, the Japan Participation Group, the Johns Hopkins University, Los Alamos National Laboratory, the Max-Planck-Institute for Astronomy (MPIA), the Max-Planck-Institute for Astrophysics (MPA), New Mexico State University, University of Pittsburgh, Princeton University, the United States Naval Observatory and the University of Washington. Also, we thank the Kottamia Center of Scientific Excellence. We thank the anonymous referee for the comments and suggestions which improved the quality of this paper.

REFERENCES

Abolfathi B. et al., 2018, ApJS, 235, 42
Akritas M. G., Bershady M. A., 1996, ApJ, 470, 706
Allen S. W., Evrard A. E., Mantz A. B., 2011, ARA&A, 49, 409
Andersson K., Peterson J. R., Madejski G., Goobar A., 2009, ApJ, 696, 1029
Andreon S., 2012, A&A, 546, A6
Arnaud M., Pointecouteau E., Pratt G. W., 2005, A&A, 441, 893
Arnaud K. A., 1996, in Jacoby G. H., Barnes J., eds, ASP Conf. Ser. Vol. 101, Astronomical Data Analysis Software and Systems V. Astron. Soc. Pac., San Francisco, p. 17
Bertin E., Arnouts S., 1996, A&AS, 117, 393
Bharadwaj V., Reiprich T. H., Lovisari L., Eckmiller H. J., 2015, A&A, 573, A75
Böhringer H. et al., 2000, ApJS, 129, 435
Böhringer H. et al., 2004, A&A, 425, 367
Böhringer H. et al., 2007, A&A, 469, 363
Cash W., 1979, ApJ, 228, 939
Clerc N. et al., 2014, MNRAS, 444, 2723(C14)
Clerc N., Sadibekova T., Pierre M., Pacaud F., Le Fèvre J.-P., Adami C., Altieri B., Valtchanov I., 2012, MNRAS, 423, 3561
Croston J. H. et al., 2008, A&A, 487, 431
Ebrahimpour L. et al., 2018, preprint (arXiv:1805.03465)
Faccioli L. et al., 2018, A&A, 620, A9
Finoguenov A. et al., 2007, ApJS, 172, 182
Giles P. A. et al., 2016, A&A, 592, A3
Gioia I. M., Maccacaro T., Schild R. E., Wolter A., Stocke J. T., Morris S. L., Henry J. P., 1990, ApJS, 72, 567
Hilton M. et al., 2012, MNRAS, 424, 2086
Horner D. J., Perlman E. S., Ebeling H., Jones L. R., Scharf C. A., Wegner G., Malkan M., Maughan B., 2008, ApJS, 176, 374
Kaiser N., 1986, MNRAS, 222, 323
Kalberla P. M. W., Burton W. B., Hartmann D., Arnal E. M., Bajaja E., Morras R., Pöppel W. G. L., 2005, A&A, 440, 775
Kotov O., Vikhlinin A., 2005, ApJ, 633, 781
Krumpe M. et al., 2008, A&A, 483, 415
Lloyd-Davies E. J. et al., 2011, MNRAS, 418, 14
Lovisari L., Reiprich T. H., Schellenberger G., 2015, A&A, 573, A118
Mantz A., Allen S. W., Rapetti D., Ebeling H., 2010a, MNRAS, 406, 1759
Mantz A., Allen S. W., Ebeling H., Rapetti D., Drlica-Wagner A., 2010b, MNRAS, 406, 1773
Maughan B. J., Jones C., Forman W., Van Speybroeck L., 2008, ApJS, 174, 117
Maughan B. J., Giles P. A., Randall S. W., Jones C., Forman W. R., 2012, MNRAS, 421, 1583
Mehrtens N. et al., 2012, MNRAS, 423, 1024
Mittal R., Hicks A., Reiprich T. H., Jaritz V., 2011, A&A, 532, A133
Pacaud F. et al., 2006, MNRAS, 372, 578
Pacaud F. et al., 2007, MNRAS, 382, 1289
Pacaud F. et al., 2016, A&A, 592, A2
Pierre M. et al., 2004, Journal of Cosmology and Astro-Particle Physics, 2004, 011
Pierre M. et al., 2016, A&A, 592, A1
Planck Collaboration et al., 2011, A&A, 536, A11
Pratt G. W., Arnaud M., 2003, A&A, 408, 1
Pratt G. W., Arnaud M., 2005, A&A, 429, 791
Pratt G. W., Croston J. H., Arnaud M., Böhringer H., 2009, A&A, 498, 361 (P09)
Reiprich T. H., Böhringer H., 2002, ApJ, 567, 716
Rozo E. et al., 2010, ApJ, 708, 645
Rykoff E. S. et al., 2014, ApJ, 785, 104
Sadibekova T., Pierre M., Clerc N., Faccioli L., Gastaud R., Le Fevre J.-P., Rozo E., Rykoff E., 2014, A&A, 571, A87
Sehgal N. et al., 2011, ApJ, 732, 44
Sun M., Voit G. M., Donahue M., Jones C., Forman W., Vikhlinin A., 2009, ApJ, 693, 1142
Takey A., Schwope A., Lamer G., 2011, A&A, 534, A120
Takey A., Schwope A., Lamer G., 2013, A&A, 558, A75
Takey A., Schwope A., Lamer G., 2014, A&A, 564, A54
Takey A., Durret F., Mahmoud E., Ali G. B., 2016, A&A, 594, A32
Takey A., Durret F., Márquez I., Ellien A., Molham M., Plat A., 2019, MNRAS, 486, 4863
Tinker J., Kravtsov A. V., Klypin A., Abazajian K., Warren M., Yepes G., Gottlöber S., Holz D. E., 2008, ApJ, 688, 709
Vikhlinin A. et al., 2009a, ApJ, 692, 1033
Vikhlinin A. et al., 2009b, ApJ, 692, 1060
Vikhlinin A., McNamara B. R., Forman W., Jones C., Quintana H., Hornstrup A., 1998, ApJ, 502, 558
Voit G. M., Kay S. T., Bryan G. L., 2005, MNRAS, 364, 909
Wen Z. L., Han J. L., Liu F. S., 2009, ApJS, 183, 197
Wilms J., Allen A., McCray R., 2000, ApJ, 542, 914
Zou S., Maughan B. J., Giles P. A., Vikhlinin A., Pacaud F., Burenin R., Hornstrup A., 2016, MNRAS, 463, 820
Šuhada R. et al., 2012, A&A, 537, A39

APPENDIX A: TABLES

Table A1. The X-CLASS-redMaPPer 92 cluster sample.

X-CLASS ID (1)	*RA* (2)	*Dec.* (2)	z_λ	z_s	*Member*(z_s) (3)
40	35.189	− 3.434	0.35	0.33	11
54	145.938	16.738	0.18	0.17	3
56	145.886	16.667	0.28	0.26	3
62	44.142	0.103	0.37	0.36	16
78	10.722	− 9.570	0.42	0.42	1
88	183.395	2.896	0.41	0.41	2
96	9.276	9.158	0.27	0.25	7
99	28.176	1.009	0.23	0.22	21
109	10.961	0.792	0.47	0.48	8
110	10.720	0.714	0.27	0.28	15
156	187.580	16.281	0.20	0.20	3
169	35.522	− 4.549	0.32	0.32	8
201	328.406	17.696	0.25	0.23	5
229	148.582	17.597	0.37	0.38	3
264	213.602	− 0.379	0.14	0.14	18
336	150.772	32.897	0.41	0.42	4
342	36.455	− 5.897	0.22	0.20	4
343	33.872	− 4.681	0.35	0.35	14
347	35.486	− 5.757	0.26	0.26	2
377	6.648	17.159	0.40	0.40	7
382	180.204	− 3.458	0.37	0.40	1
402	223.232	16.702	0.06	0.05	73
403	233.135	4.677	0.06	0.04	34
458	4.638	16.436	0.57	0.55	2
466	202.704	− 1.865	0.10	0.09	33
468	202.772	− 1.765	0.55	0.56	5
470	208.572	− 2.366	0.57	0.55	4
561	229.078	0.092	0.12	0.12	22
562	229.102	− 0.832	0.38	0.38	2
564	229.185	− 0.973	0.12	0.12	25
574	7.640	26.303	0.50	0.50	6
632	190.391	32.841	0.36	0.40	6
653	173.314	66.376	0.12	0.11	33
686	131.762	34.854	0.48	0.46	1
706	170.030	43.301	0.58	0.61	3
740	182.814	39.195	0.34	0.35	11
787	196.001	67.515	0.22	0.23	16
841	140.259	30.092	0.55	0.55	4
870	230.776	8.609	0.06	0.04	65
890	20.273	3.802	0.34	0.36	2
1059	358.902	5.855	0.28	0.28	18
1062	159.508	41.773	0.13	0.12	15
1063	201.287	65.836	0.18	0.16	4
1086	217.764	42.241	0.44	0.42	6
1159	134.057	37.936	0.41	0.41	13
1185	191.328	56.769	0.53	0.49	2
1188	213.894	28.394	0.24	0.22	2
1266	229.191	7.022	0.06	0.04	64
1282	197.945	22.028	0.17	0.17	7
1283	197.736	21.966	0.29	0.28	2
1307	7.370	− 0.214	0.06	0.06	86
1341	125.461	1.200	0.09	0.09	11
1368	154.404	59.563	0.29	0.28	19
1442	17.513	13.978	0.07	0.06	36
1443	155.544	38.523	0.07	0.06	50
1537	187.961	12.001	0.25	0.25	2
1544	121.939	39.771	0.36	0.37	4
1581	148.809	18.208	0.41	0.42	2
1627	197.135	53.704	0.35	0.33	14
1635	114.025	43.652	0.44	0.43	8
1637	154.264	39.049	0.21	0.21	22
1642	132.201	44.938	0.55	0.54	9
1676	200.182	33.154	0.29	0.30	2
1677	200.037	33.089	0.05	0.04	40
1678	145.756	46.993	0.36	0.40	13
1764	337.052	20.583	0.38	0.41	6
1813	164.233	6.978	0.32	0.30	1
1853	350.358	19.753	0.33	0.30	24
1862	190.793	14.340	0.34	0.34	1
1931	196.957	29.429	0.26	0.24	2
1944	149.044	− 0.365	0.59	0.59	3
2022	215.001	6.581	0.56	0.56	3
2051	179.602	44.091	0.40	0.41	1
2080	139.896	30.531	0.42	0.43	3
2081	140.220	30.466	0.29	0.29	5
2090	335.987	− 1.583	0.10	0.09	7
2093	335.812	− 1.661	0.30	0.30	1
2109	4.406	− 0.877	0.21	0.20	25
2113	188.483	15.437	0.23	0.23	2
2116	188.570	15.252	0.28	0.29	1
2129	329.371	− 7.800	0.07	0.06	58
2155	152.835	53.572	0.41	0.39	6
2202	340.841	− 9.597	0.44	0.44	2
2209	149.769	13.089	0.39	0.40	1
2211	189.670	9.475	0.23	0.23	3
2214	126.054	30.077	0.32	0.30	1
2295	120.607	39.091	0.35	0.37	2
2317	227.368	7.557	0.08	0.07	41
419	337.096	− 5.342	0.35	–	–
535	339.914	− 5.725	0.26	–	–
2020	214.847	6.643	0.55	–	–
2130	329.308	− 7.712	0.48	–	–

Table A1 – *continued*

Notes. (**1**) The X-ray and optical images are retrievable from the public X-CLASS database at http://xmm-lss.in2p3.fr:8080/l4sdb/.
(**2**) RA and Dec. are J2000 coordinates in degrees.
(**3**) The number of cluster members with spectroscopic redshifts.

Table A2. Characteristic X-ray properties of 57 galaxy clusters measured within R_{500}.

X-CLASS ID	T	$-eT$	$+eT$	R_{500}	$-eR_{500}$	$+eR_{500}$	F_x [0.5–2 keV]	$-eF_x$	$+eF_x$	L_x^* [0.5–2 keV]	$-eL_x$	$+eL_x$
	keV			Mpc			10^{-14} (erg s^{-1}cm^{-2})			erg s^{-1}		
40	7.24	2.31	5.24	1.14	0.22	0.41	8.52	0.80	0.41	43.45	0.032	0.031
56	5.52	0.84	0.94	0.99	0.08	0.09	23.18	0.87	0.77	43.65	0.031	0.016
62	7.35	0.46	0.46	1.14	0.04	0.04	61.41	0.73	0.74	44.42	0.006	0.006
88	4.39	0.48	0.42	0.83	0.03	0.06	18.64	0.56	0.36	44.01	0.014	0.011
110	2.16	0.38	0.48	0.64	0.06	0.07	4.51	0.22	0.43	43.05	0.040	0.036
156	5.26	0.57	0.87	1.09	0.07	0.10	43.89	1.24	1.30	43.70	0.014	0.013
169	2.64	1.17	2.64	0.51	0.26	0.37	2.48	0.23	0.19	42.90	0.049	0.042
229	2.92	0.26	0.25	0.70	0.04	0.03	24.91	0.67	0.59	44.09	0.012	0.012
264	2.62	0.45	0.27	0.78	0.07	0.04	50.13	1.29	1.25	43.41	0.011	0.011
336	4.05	0.17	0.17	0.82	0.02	0.02	28.49	0.39	0.44	44.22	0.007	0.007
342	4.14	1.43	1.70	1.09	0.20	0.33	25.58	1.34	0.94	43.47	0.022	0.029
347	1.82	0.38	0.54	0.54	0.04	0.12	6.10	0.43	0.79	43.11	0.042	0.040
377	3.91	0.10	0.11	0.80	0.01	0.01	26.47	0.25	0.23	44.15	0.005	0.005
382	5.96	0.38	0.38	1.09	0.04	0.04	22.33	0.32	0.42	44.04	0.008	0.008
458	10.13	0.25	0.25	1.22	0.02	0.02	111.34	0.64	0.66	45.05	0.003	0.003
468	6.73	0.39	0.73	1.01	0.05	0.04	18.08	0.29	0.28	44.28	0.012	0.010
470	6.19	0.75	0.93	0.92	0.06	0.07	13.53	0.42	0.26	44.15	0.014	0.013
562	4.74	0.80	1.05	0.88	0.09	0.09	9.49	0.56	0.38	43.65	0.026	0.025
574	6.64	0.42	0.56	1.01	0.04	0.05	19.41	0.28	0.37	44.21	0.005	0.009
632	6.50	0.27	0.28	1.14	0.03	0.03	53.72	0.54	0.60	44.42	0.006	0.006
706	5.62	0.31	0.29	0.87	0.02	0.03	29.76	0.40	0.46	44.59	0.007	0.007
740	5.57	0.49	0.44	1.02	0.03	0.06	34.21	0.66	0.53	44.12	0.009	0.011
787	3.36	0.11	0.19	0.84	0.02	0.02	54.10	0.52	0.60	43.92	0.006	0.005
841	2.01	0.36	0.64	0.51	0.05	0.08	2.94	0.28	0.27	43.56	0.042	0.040
890	4.97	0.91	1.79	0.97	0.11	0.16	15.39	0.66	0.41	43.79	0.017	0.016
1063	1.28	0.04	0.03	0.50	0.01	0.01	8.26	0.24	0.27	42.80	0.015	0.015
1086	4.27	2.28	3.60	0.93	0.24	0.49	4.58	0.94	0.23	43.42	0.059	0.081
1159	7.43	0.36	0.37	1.14	0.03	0.03	55.18	0.54	0.47	44.47	0.005	0.005
1188	1.75	0.12	0.40	0.56	0.02	0.07	7.23	0.48	0.83	43.04	0.040	0.037
1283	6.76	0.93	1.64	1.18	0.12	0.12	36.65	1.17	0.57	43.92	0.017	0.012
1544	8.37	1.48	2.72	1.24	0.12	0.19	30.50	0.96	1.32	44.11	0.018	0.020
1627	3.09	0.18	0.18	0.70	0.02	0.02	13.26	0.22	0.22	43.66	0.010	0.010
1635	4.60	0.56	0.66	0.89	0.06	0.07	12.94	0.45	0.33	43.93	0.017	0.017
1642	2.12	0.35	0.34	0.56	0.05	0.04	3.84	0.17	0.18	43.66	0.024	0.026
1676	2.53	0.18	0.18	0.68	0.03	0.03	10.13	0.30	0.26	43.45	0.013	0.013
1764	5.26	0.67	1.13	1.01	0.07	0.15	8.37	0.32	0.27	43.68	0.021	0.018
1853	4.58	0.36	0.39	0.88	0.04	0.04	21.56	0.46	0.42	43.80	0.010	0.010
1862	2.25	0.28	0.47	0.56	0.05	0.04	4.10	0.23	0.25	43.21	0.027	0.026
1931	3.01	0.14	0.14	0.73	0.02	0.02	36.20	0.48	0.46	43.79	0.006	0.006
1944	3.88	1.03	1.37	0.71	0.11	0.12	3.52	0.24	0.19	43.66	0.039	0.039
2022	3.67	0.28	0.26	0.71	0.03	0.03	7.88	0.20	0.16	43.96	0.011	0.011
2051	4.24	0.83	1.18	0.84	0.09	0.12	4.45	0.32	0.23	43.38	0.028	0.026
2080	3.39	0.25	0.19	0.75	0.03	0.02	18.56	0.38	0.22	44.06	0.007	0.009
2081	3.20	0.14	0.14	0.77	0.02	0.02	31.02	0.49	0.37	43.91	0.006	0.006
2093	4.14	0.41	0.52	0.87	0.05	0.06	22.97	0.69	0.66	43.81	0.015	0.014
2155	6.20	1.51	2.08	0.98	0.13	0.16	7.92	0.44	0.26	43.56	0.025	0.023
2209	3.26	0.35	0.45	0.74	0.04	0.05	9.64	0.38	0.23	43.71	0.017	0.017
2214	2.32	0.26	0.78	0.56	0.04	0.08	4.88	0.31	0.21	43.17	0.025	0.028
2295	2.77	0.23	0.46	0.71	0.03	0.06	24.55	1.06	1.00	44.07	0.020	0.019
1678	5.73	0.15	0.15	1.07	0.02	0.02	59.17	0.41	0.43	44.47	0.003	0.003
2109	4.70	0.18	0.19	0.96	0.02	0.02	73.73	0.67	0.68	43.94	0.004	0.004
2202	8.12	0.08	0.08	1.18	0.01	0.01	153.06	0.36	0.44	44.99	0.001	0.001
2211	3.72	0.19	0.19	0.86	0.02	0.02	40.80	0.58	0.54	43.78	0.003	0.006
419	4.20	0.87	0.66	0.92	0.10	0.07	7.00	0.25	0.25	43.45	0.018	0.023
535	3.00	0.25	0.25	0.74	0.05	0.03	24.95	0.71	0.49	43.71	0.012	0.011
2020	4.82	0.43	0.44	0.83	0.04	0.04	12.67	0.32	0.21	44.13	0.013	0.013
2130	1.87	0.19	0.25	0.51	0.03	0.04	4.17	0.22	0.34	43.58	0.030	0.028

Note: * Luminosity and uncertainty are given using a base 10 logarithmic scale.

Table A3. Characteristic X-ray properties of 70 galaxy clusters measured within $R_{\rm fit}$.

X-CLASS ID	$R_{\rm fit}$	T	*-eT*	*+ eT*	F_x [0.5–2 keV]	$-eF_x$	$+eF_x$	L_x^* [0.5–2 keV]	$-eL_x$	$+eL_x$
	arcsec	keV			10^{-14} erg s^{-1}cm^{-2}			erg s^{-1}		
40	75.0	2.07	0.25	0.41	3.79	0.26	0.24	43.15	0.028	0.027
54	150.0	2.55	0.24	0.35	10.77	0.42	0.27	42.92	0.016	0.016
56	212.5	5.07	0.61	0.95	21.66	0.79	0.69	43.62	0.015	0.015
62	212.5	6.86	0.36	0.49	60.10	0.94	0.57	44.41	0.006	0.007
78	75.0	8.68	2.53	6.69	4.29	0.54	0.22	43.38	0.040	0.040
88	162.5	4.17	0.32	0.56	18.96	0.34	0.45	44.01	0.013	0.012
109	87.5	3.79	0.74	1.16	3.90	0.26	0.24	43.49	0.033	0.031
110	137.5	3.05	0.73	1.18	4.73	0.45	0.29	43.05	0.036	0.034
156	275.5	5.10	0.56	0.70	41.75	1.38	1.11	43.67	0.013	0.013
169	75.0	5.32	1.54	3.03	2.38	0.19	0.08	42.87	0.040	0.036
229	187.5	2.94	0.25	0.25	29.70	0.52	0.77	44.17	0.012	0.012
264	237.5	2.94	0.27	0.23	42.13	0.92	0.89	43.33	0.010	0.010
336	212.5	4.59	0.25	0.25	33.37	0.38	0.51	44.28	0.007	0.007
342	150.0	3.11	0.48	0.56	14.89	0.76	0.63	43.25	0.021	0.020
343	125.0	4.67	0.74	1.08	12.03	0.67	0.53	43.66	0.021	0.021
347	112.5	3.79	1.43	2.04	6.05	0.49	0.55	43.08	0.040	0.035
377	225.0	3.66	0.11	0.11	32.67	0.29	0.28	44.24	0.005	0.005
382	175.0	6.25	0.37	0.37	20.42	0.31	0.31	44.00	0.008	0.008
468	62.5	5.12	0.55	0.72	5.64	0.15	0.21	43.79	0.019	0.019
470	112.5	7.25	1.09	1.08	11.28	0.39	0.16	44.07	0.014	0.013
562	112.5	3.39	0.31	0.44	9.12	0.40	0.26	43.65	0.018	0.017
574	175.0	6.69	0.42	0.60	20.24	0.28	0.36	44.23	0.009	0.009
632	225.0	6.30	0.27	0.28	55.16	0.61	0.64	44.43	0.006	0.006
686	62.5	3.91	1.50	2.65	3.47	0.54	0.29	43.41	0.055	0.054
706	225.0	6.06	0.31	0.32	37.94	0.58	0.49	44.69	0.007	0.007
740	162.5	5.80	0.43	0.44	30.13	0.54	0.46	44.06	0.009	0.009
787	200.0	3.62	0.15	0.15	48.15	0.58	0.61	43.86	0.006	0.006
841	78.5	1.99	0.33	0.56	2.96	0.25	0.31	43.57	0.042	0.040
890	150.0	4.87	0.87	1.31	12.46	0.43	0.33	43.70	0.016	0.016
1059	112.5	13.56	4.60	8.49	5.54	0.41	0.27	43.10	0.028	0.027
1062	225.0	3.11	0.22	0.22	25.36	0.38	0.67	43.00	0.009	0.009
1063	112.5	1.28	0.04	0.04	5.99	0.20	0.16	42.66	0.016	0.015
1086	87.5	5.31	1.24	1.33	5.92	0.47	0.40	43.53	0.030	0.031
1159	225.0	7.58	0.37	0.37	57.11	0.71	0.47	44.49	0.005	0.005
1185	87.5	27.88	18.95	− 27.30	3.08	3.08	0.34	43.34	0.065	0.062
1188	87.5	3.13	0.59	0.64	8.16	0.42	0.38	43.07	0.024	0.023
1282	237.5	3.87	0.19	0.19	52.13	0.79	0.69	43.61	0.007	0.006
1283	225.0	6.63	0.82	1.19	34.97	1.11	0.62	43.90	0.014	0.013
1307	162.5	5.07	0.62	1.13	34.44	0.88	0.73	42.48	0.011	0.011
1537	62.5	4.58	0.44	0.53	15.59	0.42	0.49	43.45	0.016	0.015
1544	225.0	10.38	2.05	4.58	29.95	1.04	0.79	44.10	0.018	0.021
1581	37.5	7.57	2.96	8.19	1.87	0.25	0.11	43.01	0.049	0.046
1627	162.5	3.15	0.18	0.19	14.22	0.23	0.23	43.69	0.010	0.010
1635	150.0	4.66	0.55	0.64	12.93	0.37	0.36	43.93	0.017	0.016
1642	112.5	2.55	0.35	0.73	4.72	0.30	0.22	43.74	0.030	0.024
1676	112.5	2.96	0.26	0.26	8.13	0.23	0.20	43.35	0.014	0.014
1764	162.5	4.57	0.87	0.70	7.47	0.25	0.21	43.63	0.019	0.024
1813	137.5	11.77	4.19	33.04	4.74	0.63	0.38	43.08	0.044	0.031
1853	187.5	4.48	0.33	0.38	22.01	0.37	0.52	43.80	0.010	0.010
1862	75.0	1.58	0.10	0.10	3.54	0.18	0.22	43.16	0.023	0.023
1931	287.5	2.89	0.17	0.17	38.10	0.52	0.49	43.82	0.007	0.007
1944	100.0	3.26	0.63	1.22	3.47	0.37	0.17	43.66	0.035	0.040
2022	125.0	3.34	0.19	0.42	8.49	0.21	0.19	44.00	0.015	0.011
2051	100.0	3.16	0.40	0.54	4.55	0.22	0.17	43.40	0.019	0.019
2080	125.0	3.75	0.18	0.18	18.91	0.27	0.19	44.06	0.007	0.007
2081	300.0	2.87	0.17	0.18	35.37	0.64	0.54	43.97	0.004	0.007
2093	150.0	4.04	0.32	0.35	22.96	0.66	0.59	43.81	0.012	0.011
2116	275.0	4.09	0.34	0.45	28.55	0.76	0.72	43.85	0.012	0.011
2155	125.0	9.78	2.73	4.38	6.46	0.43	0.22	43.46	0.022	0.022
2209	162.5	3.60	0.50	0.54	10.19	0.41	0.29	43.73	0.018	0.019
2214	150.0	1.57	0.14	0.13	5.46	0.24	0.40	43.24	0.028	0.027
2295	200.0	2.16	0.15	0.18	37.51	1.48	1.96	44.27	0.017	0.019

Table A3 – *continued*

X-CLASS ID	$R_{\rm fit}$	T	*-eT*	*+ eT*	F_x [0.5–2 keV]	$-eF_x$	$+eF_x$	L_x^* [0.5–2 keV]	$-eL_x$	$+eL_x$
	arcsec	keV			10^{-14} erg s^{-1}cm^{-2}			erg s^{-1}		
1678	200.0	5.72	0.15	0.15	59.36	0.40	0.41	44.47	0.003	0.003
2109	225.0	4.53	0.17	0.17	63.71	0.57	0.45	43.88	0.004	0.004
2113	250.0	5.13	0.13	0.13	84.79	0.54	0.57	44.12	0.003	0.003
1677	75.0	0.96	0.02	0.02	4.75	0.16	0.12	41.22	0.014	0.014
419	112.5	3.38	0.35	0.54	4.79	0.17	0.12	43.30	0.021	0.019
535	300.0	2.03	0.11	0.11	34.51	1.20	0.75	43.87	0.012	0.011
2020	137.5	4.55	0.45	0.47	12.58	0.33	0.30	44.13	0.014	0.014
2130	62.5	2.00	0.21	0.24	3.65	0.24	0.18	43.52	0.027	0.026

Note: * Luminosity and uncertainty are given using a base 10 logarithmic scale.

Table A4. Characteristic X-ray properties of 92 galaxy clusters measured within $R_{300\,\rm kpc}$.

X-CLASS ID	$R_{300\,\rm kpc}$	T	*-eT*	*+ eT*	F_x [0.5–2 keV]	$-eF_x$	$+eF_x$	L_x^* [0.5–2 keV]	$-eL_x$	$+eL_x$
	arcsec	keV			10^{-14} erg s^{-1} cm^{-2}			erg s^{-1}		
40	60.34	1.93	0.22	0.27	3.27	0.18	0.22	43.09	0.029	0.028
54	96.87	2.22	0.15	0.35	7.69	0.27	0.25	42.78	0.017	0.016
56	71.18	3.02	0.33	0.37	7.25	0.34	0.29	43.16	0.019	0.019
62	58.48	5.64	0.30	0.34	29.38	0.46	0.36	44.11	0.008	0.008
78	54.11	8.26	2.74	6.84	3.24	0.35	0.22	43.26	0.022	0.043
88	54.90	5.15	0.49	0.56	7.48	0.24	0.20	43.60	0.015	0.015
96	72.69	10.4	0.31	0.31	97.31	0.58	0.69	44.26	0.003	0.003
99	82.29	6.32	0.15	0.15	134.3	0.80	1.00	44.26	0.003	0.003
109	50.80	3.42	0.70	1.06	2.28	0.18	0.15	43.26	0.039	0.038
110	72.24	3.57	0.81	1.24	2.85	0.26	0.18	42.83	0.035	0.035
156	91.94	5.32	0.51	0.84	18.22	0.73	0.52	43.31	0.015	0.014
169	64.12	10.47	4.28	9.03	2.06	0.19	0.17	42.78	0.040	0.021
201	76.73	11.35	0.40	0.40	326.59	1.29	1.71	44.71	0.002	0.002
229	58.32	2.23	0.28	0.61	3.10	0.23	0.17	43.21	0.034	0.032
264	123.26	2.61	0.23	0.44	13.67	0.34	0.51	42.85	0.015	0.015
336	55.02	4.43	0.21	0.22	18.47	0.34	0.18	44.02	0.008	0.008
342	83.60	3.19	0.41	0.57	10.32	0.47	0.28	43.09	0.020	0.073
343	60.49	3.57	0.55	0.61	7.27	0.32	0.25	43.45	0.022	0.021
347	74.23	2.17	0.35	0.61	4.58	0.29	0.43	42.98	0.038	0.036
377	55.69	4.24	0.12	0.15	15.17	0.19	0.14	43.90	0.006	0.006
382	58.96	5.28	0.31	0.45	9.44	0.19	0.15	43.67	0.010	0.009
402	271.03	2.05	0.02	0.02	235.23	0.73	0.97	43.09	0.002	0.002
403	242.45	2.11	0.02	0.02	158.43	1.03	0.57	42.80	0.002	0.002
458	45.93	10.80	0.36	0.53	41.23	0.33	0.36	44.62	0.004	0.004
466	170.13	4.36	0.07	0.07	186.16	1.06	0.64	43.56	0.002	0.002
468	46.69	4.45	0.53	0.62	5.04	0.20	0.18	43.75	0.021	0.021
470	45.91	8.73	0.88	1.71	5.06	0.15	0.14	43.71	0.017	0.015
561	137.83	5.80	0.10	0.10	203.54	0.94	0.76	43.90	0.002	0.002
562	58.10	2.60	0.18	0.21	7.15	0.31	0.17	43.56	0.015	0.015
564	141.58	4.87	0.12	0.12	82.88	0.63	0.74	43.51	0.003	0.003
574	49.05	6.21	0.43	0.44	9.12	0.16	0.17	43.89	0.010	0.010
632	59.37	6.28	0.38	0.39	18.17	0.31	0.3	43.95	0.009	0.008
653	137.64	5.15	0.12	0.12	206.91	1.21	1.19	43.83	0.003	0.003
686	50.33	2.05	0.39	0.73	3.02	0.23	0.25	43.40	0.046	0.043
706	45.43	5.58	0.26	0.31	17.46	0.29	0.27	44.36	0.004	0.008
740	61.90	5.64	0.45	0.47	17.54	0.32	0.37	43.83	0.011	0.011
787	84.25	6.67	0.41	0.54	20.40	0.40	0.37	43.47	0.008	0.008
841	46.83	2.51	0.47	0.73	2.15	0.18	0.19	43.41	0.046	0.043
890	61.76	4.37	0.44	0.69	7.15	0.24	0.23	43.46	0.016	0.015
1059	70.40	3.26	0.69	1.26	3.21	0.24	0.21	42.91	0.036	0.031
1062	127.43	2.50	0.17	0.17	15.40	0.46	0.21	42.79	0.011	0.011

Table A4 – *continued*

X-CLASS ID	$R_{300\,\mathrm{kpc}}$ arcsec	T keV	*-eT*	*+ eT*	F_x [0.5–2 keV] 10^{-14} erg s^{-1} cm^{-2}	$-eF_x$	$+eF_x$	L_x^* [0.5–2 keV] erg s^{-1}	$-eL_x$	$+eL_x$
1063	98.67	1.22	0.05	0.04	4.16	0.18	0.16	42.50	0.018	0.017
1086	52.61	2.96	0.71	0.88	4.44	0.43	0.27	43.43	0.035	0.036
1159	55.07	8.21	0.48	0.57	18.90	0.33	0.32	44.00	0.008	0.008
1185	47.80	22.64	14.93	− 22.64	1.91	1.91	0.29	43.13	0.079	0.069
1188	79.91	2.35	0.40	0.60	5.17	0.33	0.32	42.88	0.028	0.027
1282	103.40	3.78	0.19	0.20	31.73	0.47	0.46	43.40	0.007	0.007
1283	69.55	5.23	0.41	0.63	26.47	0.71	0.54	43.78	0.012	0.010
1307	162.50	0.00	0.00	0.00	0.00	0.00	0.00	42.82	0.007	0.008
1341	180.97	3.73	0.10	0.10	111.20	1.10	0.80	43.35	0.004	0.004
1368	69.11	7.88	0.84	0.90	29.60	0.64	0.52	43.82	0.010	0.009
1442	226.97	2.92	0.11	0.11	87.11	1.23	0.71	42.93	0.005	0.005
1443	227.88	2.31	0.06	0.06	123.47	0.97	0.83	43.00	0.004	0.004
1537	77.30	4.95	0.59	0.67	16.60	0.44	0.70	43.48	0.017	0.017
1544	59.27	6.28	1.09	1.65	11.91	0.67	0.49	43.72	0.026	0.025
1581	55.00	6.26	2.07	4.44	2.59	0.35	0.22	43.15	0.045	0.041
1627	60.53	3.29	0.20	0.28	7.21	0.14	0.16	43.40	0.011	0.011
1635	52.85	4.56	0.42	0.49	8.07	0.30	0.25	43.73	0.015	0.015
1642	46.85	2.44	0.31	0.38	2.65	0.12	0.13	43.49	0.024	0.021
1676	68.84	3.18	0.28	0.31	5.32	0.19	0.11	43.16	0.015	0.015
1764	57.97	2.37	0.43	0.61	1.48	0.12	0.09	42.97	0.036	0.035
1813	63.92	3.68	0.74	1.02	2.86	0.22	0.17	42.89	0.031	0.030
1853	63.42	4.57	0.30	0.32	13.10	0.20	0.29	43.58	0.010	0.009
1862	62.18	1.54	0.11	0.10	3.31	0.20	0.20	43.13	0.023	0.023
1931	74.88	3.36	0.11	0.19	26.94	0.38	0.24	43.66	0.006	0.005
1944	45.31	3.33	0.61	0.82	2.15	0.17	0.13	43.46	0.035	0.034
2022	46.40	4.13	0.29	0.33	4.36	0.10	0.11	43.70	0.013	0.013
2051	55.64	3.69	0.47	0.44	3.81	0.14	0.09	43.32	0.017	0.016
2080	53.99	4.15	0.16	0.16	12.94	0.16	0.18	43.89	0.007	0.007
2081	68.92	3.95	0.20	0.20	13.83	0.21	0.22	43.55	0.008	0.008
2093	67.76	3.50	0.21	0.35	7.79	0.21	0.23	43.34	0.015	0.014
2116	70.66	7.94	1.10	1.40	11.06	0.36	0.39	43.42	0.015	0.015
2155	55.07	5.40	1.06	1.53	2.82	0.15	0.14	43.12	0.025	0.024
2209	56.70	0.04	0.43	0.44	5.58	0.25	0.21	43.46	0.018	0.017
2214	64.71	2.46	0.63	0.91	2.91	0.21	0.16	42.94	0.030	0.028
2295	60.65	7.82	1.60	2.12	12.14	0.67	0.39	43.71	0.023	0.022
1637	89.11	6.45	0.09	0.10	220.69	0.69	0.61	44.40	0.002	0.002
1678	59.80	5.88	0.24	0.24	17.88	0.22	0.20	43.95	0.006	0.006
2090	165.01	4.67	0.11	0.11	102.67	0.67	0.73	43.32	0.003	0.003
2109	86.18	4.25	0.11	0.14	42.85	0.43	0.39	43.71	0.004	0.005
2113	82.25	5.46	0.18	0.22	34.89	0.34	0.30	43.73	0.005	0.005
2129	229.67	3.86	0.11	0.11	85.59	0.66	0.70	42.87	0.004	0.004
2202	52.86	8.57	0.13	0.24	44.56	0.18	0.18	44.45	0.003	0.002
2211	82.24	4.09	0.23	0.24	15.41	0.40	0.23	43.36	0.009	0.009
2317	202.55	4.19	0.09	0.09	71.46	0.44	0.51	42.98	0.003	0.003
870	247.40	4.02	0.04	0.04	1130.10	5.10	2.90	43.59	0.001	0.001
1266	259.30	3.28	0.02	0.02	1965.10	4.10	3.90	43.91	0.001	0.001
1677	282.71	1.02	0.02	0.02	17.43	0.43	0.37	41.78	0.010	0.010
419	60.60	2.81	0.29	0.32	3.55	0.15	0.11	43.18	0.019	0.020
535	74.68	0.02	0.22	0.23	13.95	0.34	0.40	43.46	0.012	0.012
2020	46.66	5.57	0.53	0.50	7.61	0.14	0.14	43.91	0.015	0.012
2130	50.34	0.05	0.22	0.25	3.25	0.18	0.16	43.46	0.027	0.027

Note: * Luminosity and uncertainty are given using a base 10 logarithmic scale.

Table A5. Temperature measurements for 22 XC1 in the literature.

	Published results					Our results					
X-CLASS ID	$T_{\rm published}$ keV	$-eT_{\rm published}$	$+eT_{\rm published}$	*Status*	*Ref*	T_{500} keV	$-eT_{500}$	$+eT_{500}$	R_{500} arcsec	$-eR_{500}$	$+eR_{500}$
96	6.50	0.70	1.00	[0.15–1] R_{500}	6	–	–	–	–	–	–
99	4.60	0.40	0.50	[0.15–1] R_{500}	6	–	–	–	–	–	–
201	8.68	0.27	0.29	90% of SI	1	–	–	–	–	–	–
402	2.18	0.16	0.19	[0.35] $R200$	2	–	–	–	–	–	–
403	2.58	0.15	0.15	[0.1–0.3] $R200$	3	–	–	–	–	–	–
458	8.90	0.03	0.03	no-core R_{500}	5	10.13	0.25	0.25	189.34	2.51	2.49
466	4.45	0.13	0.13	90% of SI	1	–	–	–	–	–	–
561	5.25	0.15	0.16	90% of SI	1,4	–	–	–	–	–	–
564	3.40	0.08	0.08	[0.15–1] R_{500}	4	–	–	–	–	–	-
653	6.59	0.42	0.46	90% of SI	1	–	–	–	–	–	–
1341	3.69	0.24	0.29	90% of SI	1	–	–	–	–	–	–
1368	–	–	–	No *XMM* study	0	–	–	–	–	–	–
1442	–	–	–	No study	0	–	–	–	–	–	–
1443	–	–	–	No *XMM* study	0	–	–	–	–	–	–
1637	6.43	0.19	0.22	90% of SI	1	–	–	–	–	–	–
2090	–	–	–	No *XMM* study	0	–	–	–	–	–	–
2129	2.30	0.06	0.10	[0.15–1] R_{500}	4	–	–	–	–	–	–
2202	7.98	0.12	0.12	[0.15–0.75] R_{500}	7	8.11	0.08	0.08	206.78	1.15	1.15
2211	–	–	–	No study	0	3.72	0.19	0.19	236.25	6.63	6.57
2317	–	–	–	No *XMM* study	0	–	–	–	–	–	–
870	–	–	-	No *XMM* study	0	–	–	–	–	–	–
1266	–	–	–	No *XMM* study	0	–	–	–	–	–	–

Note: References: 1 – Andersson et al. (2009); 2 – Pratt & Arnaud (2003); 3 – Pratt & Arnaud (2005); 4 – Croston et al. (2008); 5 – Kotov & Vikhlinin (2005); 6 – Maughan et al. (2008); 7 – Planck Collaboration et al. (2011).

APPENDIX B: R_{500} REPRESENTATIVE PLOTS

We present here an example of the representative plots we created through the R_{500} calculation pipeline.

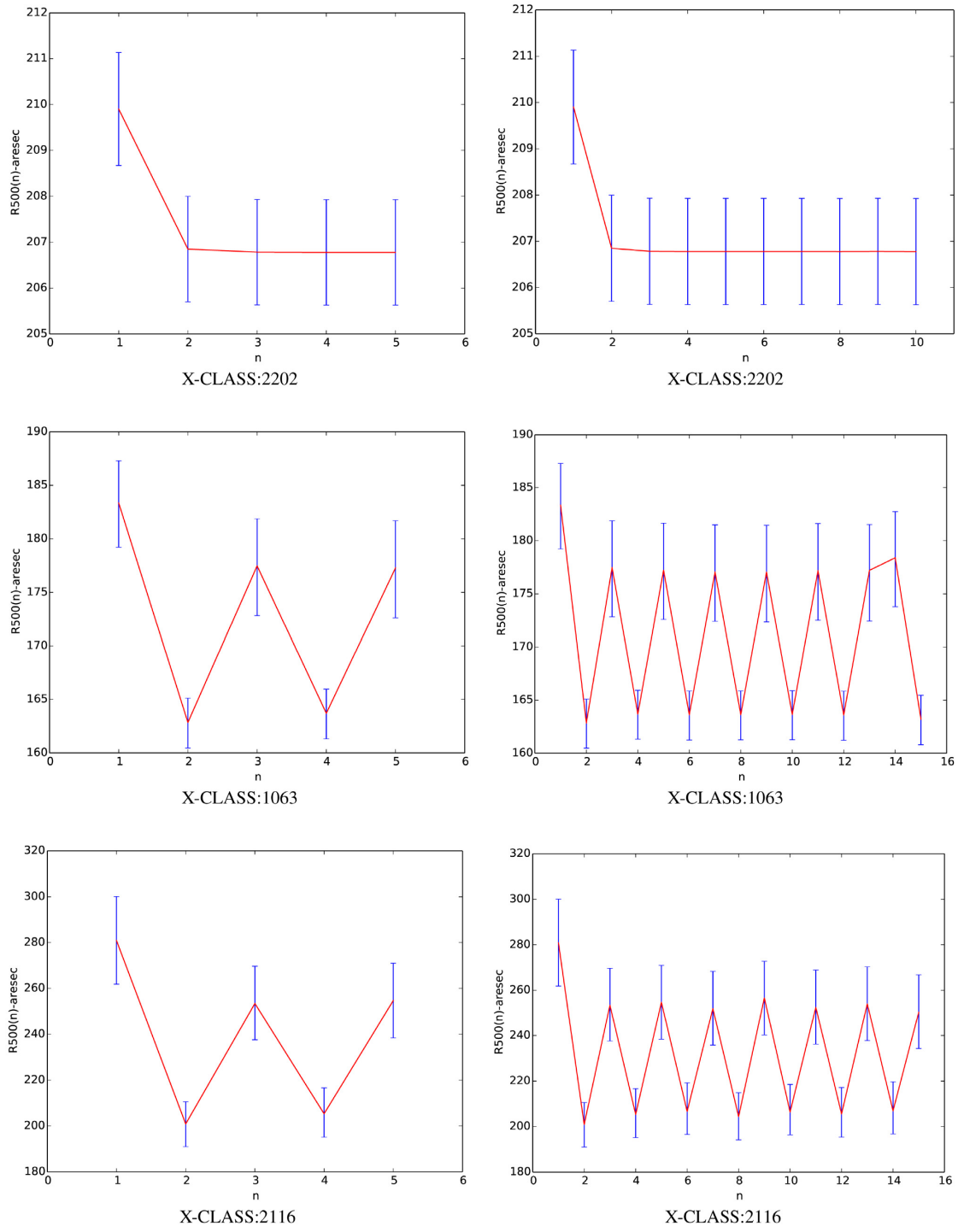

Figure B1. Representative graph of R_{500} iteration process. The x-axis represents the frequency of the iteration process, the y-axis represents R_{500} in arcsec and the blue line represents the R_{500} result within its uncertainty. Upper panel (X-CLASS:2202): (left) the results of five iteration steps and (right) the results of 10 iteration steps. This panel shows that we can pick any of the R_{500} values, since it shows stable behaviour, and we can end the iteration process for that cluster. Middle panel (X-CLASS:1063): (left) the results of five iteration steps and (right) the results of 16 iteration steps. This panel shows that we can pick only the value of R_{500} at point 14, since it did not show stable behaviour until after 14 iteration steps and then diverged again. Bottom panel (X-CLASS:2116): (left) the results of five iteration steps and (right) the results of 15 iteration steps. This panel shows a failure case, where we were unable to find a stable value for R_{500}. A colour version is available online.

This paper has been typeset from a TEX/LATEX file prepared by the author.